



Continuously released Zn²⁺ in 3D-printed PLGA/β-TCP/Zn scaffolds for bone defect repair by improving osteoinductive and anti-inflammatory properties

Chunxu Li^{a,1}, Fengbo Sun^{b,1}, Jingjing Tian^{c,1}, Jiahao Li^a, Haidan Sun^d, Yong Zhang^e, Shigong Guo^f, Yuanhua Lin^b, Xiaodan Sun^{b,**}, Yu Zhao^{a,*}

^a Department of Orthopedics, Peking Union Medical College Hospital, Chinese Academy of Medical Sciences and Peking Union Medical College, Beijing, 100730, China

^b State Key Laboratory of Advanced Ceramics and Fine Processing, School of Materials, Tsinghua University, Beijing, China

^c Medical Science Research Center, Peking Union Medical College Hospital, Chinese Academy of Medical Sciences and Peking Union Medical College, Beijing, China

^d Core Facility of Instrument, Institute of Basic Medical Sciences, Chinese Academy of Medical Sciences and School of Basic Medicine, Peking Union Medical College, Beijing, China

^e The State Key Laboratory of Medical Molecular Biology, Institute of Basic Medical Sciences, Chinese Academy of Medical Sciences and School of Basic Medicine, Peking Union Medical College, Beijing, China

^f Department of Rehabilitation Medicine, Southmead Hospital, Bristol, UK

ARTICLE INFO

Keywords:

3D printing
Zinc submicron particles
Osteoinductivity
Anti-inflammatory
Bone defect repair

ABSTRACT

Long-term nonunion of bone defects has always been a major problem in orthopedic treatment. Artificial bone graft materials such as Poly (lactic-co-glycolic acid)/β-tricalcium phosphate (PLGA/β-TCP) scaffolds are expected to solve this problem due to their suitable degradation rate and good osteoconductivity. However, insufficient mechanical properties, lack of osteoinductivity and infections after implanted limit its large-scale clinical application. Hence, we proposed a novel bone repair bioscaffold by adding zinc submicron particles to PLGA/β-TCP using low temperature rapid prototyping 3D printing technology. We first screened the scaffolds with 1 wt % Zn that had good biocompatibility and could stably release a safe dose of zinc ions within 16 weeks to ensure long-term non-toxicity. As designed, the scaffold had a multi-level porous structure of biomimetic cancellous bone, and the Young's modulus (63.41 ± 1.89 MPa) and compressive strength (2.887 ± 0.025 MPa) of the scaffold were close to those of cancellous bone. In addition, after a series of *in vitro* and *in vivo* experiments, the scaffolds proved to have no adverse effects on the viability of BMSCs and promoted their adhesion and osteogenic differentiation, as well as exhibiting higher osteogenic and anti-inflammatory properties than PLGA/β-TCP scaffold without zinc particles. We also found that this osteogenic and anti-inflammatory effect might be related to Wnt/β-catenin, P38 MAPK and NFκB pathways. This study lay a foundation for the follow-up study of bone regeneration mechanism of Zn-containing biomaterials. We envision that this scaffold may become a new strategy for clinical treatment of bone defects.

1. Introduction

Bone defects usually occur in a variety of orthopedic diseases. Long-term non-union of bone defects can lead to physical disability, and the economic burden caused by the loss of an individual's ability to work is detrimental to both the individual and society [1]. Therefore, the

treatment of bone defects is particularly important, and one of the most effective treatment methods is bone grafting. However, natural bone grafts such as autologous and allograft bone are subject to infection and disease transmission, thus we urgently need to develop more optimal bone grafts to solve these clinical problems [2,3]. And artificial bone grafts designed by various new technologies may be more ideal bone

Peer review under responsibility of KeAi Communications Co., Ltd.

* Corresponding author.

** Corresponding author.

E-mail addresses: sunxiaodan@tsinghua.edu.cn (X. Sun), zhaoyupumch@163.com (Y. Zhao).

¹ These authors contributed equally to this work.

<https://doi.org/10.1016/j.bioactmat.2022.12.015>

Received 5 August 2022; Received in revised form 15 December 2022; Accepted 18 December 2022

2452-199X/© 2022 The Authors. Publishing services by Elsevier B.V. on behalf of KeAi Communications Co. Ltd. This is an open access article under the CC BY-NC-ND license (<http://creativecommons.org/licenses/by-nc-nd/4.0/>).

grafts at present [4]. In recent years, poly (lactic-co-glycolic acid)/ β -tricalcium phosphate (PLGA/ β -TCP) composite has been considered to be an excellent artificial bone graft material due to its osteogenesis capacity, suitable degradation rate and bio-safety properties [5–7]. However, the insufficient mechanical properties [8] and the lack of osteoinductivity [6], together with the acidic degradation products of PLGA that induce inflammation [9] jointly limit its further clinical application. Thus, many researchers were enthused to improve the biomechanical, osteogenic and anti-inflammatory properties of PLGA/ β -TCP scaffolds.

Through researches of degradable metal bone implants, it is found that metal elements such as magnesium (Mg) and zinc (Zn) can be manufactured into orthopedic implants and achieve excellent mechanical properties [10–14]. Some researchers have added Mg particles to PLGA/ β -TCP scaffold to improve the mechanical properties [15]. At the same time, the degradation of Mg and Zn metals *in vivo* can release Mg^{2+} and Zn^{2+} that beneficial to osteogenesis, thereby improving the osteoinductivity of scaffolds [16]. Compared with loading growth factors such as BMP-2 and FGF-2 to PLGA/ β -TCP scaffolds to improve osteoinductivity [17,18], adding Mg and Zn elements is costless, more safer, and avoid heterotopic ossification [19]. Nonetheless, Mg releases hydrogen during its degradation *in vivo* will result in of rapid degradation [20]. The degradation rate of Zn is more moderate than Mg [21]. Therefore, adding Zn to PLGA/ β -TCP may be a better choice.

However, the threshold concentration of Zn ions (Zn^{2+}) *in vivo* is low [22]. Although bulk zinc has strong mechanical properties, a large amount of Zn left in the body may cause toxicity once degraded, which is a safety hazard [23]. It is necessary to add smaller-sized Zn particles to PLGA/ β -TCP to ensure that the released Zn^{2+} after Zn degradation is biosafe and also has a mechanical strength similar to that of bone. At present, there are few studies on adding Zn particles to PLGA/ β -TCP for bone tissue engineering. But many studies have confirmed that the addition of Zn particles to polymers have impact on the cytotoxicity [24], structure [25], osteoinductivity [26], and anti-inflammatory effects [27] of polymers. However, the fabrication technology of Zn containing polymers were diversified. For example, the electrostatic spinning technology can mimic the extracellular matrix structure and thus facilitate cell proliferation, but the mechanical properties of the scaffolds are very low [24]. In contrast, the freeze-drying and sintering technologies could produce scaffolds with good mechanical properties and porous structures, but the structure is not controllable [25,26,28]. The selective laser sintering technology can fabricate scaffolds with controllable structure, but the high temperature can adversely affect the activity and long-term release of Zn^{2+} [29]. To solve the above problems, we proposed to use a low-temperature rapid prototyping (LT-RP) 3D printing technology to fabricate scaffolds. By comparing with other fabrication technologies (Table S1), we found that LT-RP 3D printing technology could improve the mechanical properties of fabricated scaffolds. Moreover, the scaffold had a structure that mimicked cancellous bone and could release Zn^{2+} stably over a longer period of time. Therefore, this study was proposed to incorporate Zn submicron particles (Zn-SPs, 400 nm) into the PLGA/ β -TCP by LT-RP 3D printing technology for continuously and safely release Zn^{2+} . Ultimately, this long-term release of Zn^{2+} made the scaffold had osteogenic and anti-inflammatory effects, suggesting that the scaffold is suitable for bone repair. Considering that the osteogenic and anti-inflammatory mechanisms of Zn-added polymers are currently unknown, there are no studies on the anti-inflammatory mechanisms of Zn-SPs-containing scaffolds [30,31]. We further explored the possible mechanisms by which Zn-SPs-containing PLGA/ β -TCP scaffolds affect osteogenic differentiation and inflammatory responses by proteomic analysis. Therefore, this study not only laying a foundation for Zn and Zn containing polymers on bone repair mechanisms, but also for the clinical applications of Zn-containing biomaterials.

2. Materials and methods

2.1. Fabrication of 3D-printed scaffolds

A medical-grade PLGA polymer (Glycolide (GA): Lactide (LA) ratio of 85:15, Jinan Daigang Biomaterial Co., Ltd., Shandong, China) was dissolved in 1,4-dioxane reagent (Sinopharm Chemical Reagent Co., Ltd., Shanghai, China). Different proportions of medical-grade β -TCP particles (Beijing Deke Daojin Technology Co., Ltd., Beijing, China) and medical-grade Zn-SPs at a particle size of 400 nm (nm) (Beijing Zhongke Yanuo New Material Technology Co., Ltd., Beijing, China) were added and stirred slowly for 12 h to form a homogeneous suspension. Pure PLGA (P), PLGA/ β -TCP (w/w of 4:1, 3:1, 2:1) and PLGA/ β -TCP/Zn (Zn content of 1 wt%, 2 wt%, 3 wt%, 4 wt%) were used to fabricate eight sets of scaffolds.

According to previous studies, pore size of 500–600 μ m and porosity of 60–70% in 3D printed Ti6Al4V scaffolds are optimal design parameters for promoting osteogenesis [32]. Therefore, to ensure that the mechanical properties of the scaffold were sufficient, the scaffold structure was designed according to the following structural parameters: pore size = 500 μ m, porosity = 60%. Porous scaffolds were fabricated at -10 °C by low-temperature rapid prototyping 3D printing technology (BioScaffolder3.2, Gesim, Germany). Low-temperature 3D printing technology has been shown to have advantages in the multilevel porous structure of biomimetic cancellous bone [33]. The shapes and sizes of the scaffolds remained consistent within each group. After the scaffold was fabricated, it was lyophilized in a freeze dryer (FD-1A-50, Shanghai Yuming Instrument Co., Ltd., Shanghai, China) for 48 h, and then dried in a vacuum oven at 37 °C for 7 days to completely remove the residual solvent 1,4-dioxane. Before the biological experiments were conducted, the scaffolds were immersed in a 75% ethanol solution to remove residual organic solvents and then sterilized by UV irradiation. The scaffolds were then soaked in sterile phosphate buffer saline (PBS) to remove the residual ethanol solution, and then used in both *in vitro* and *in vivo* experiments.

2.2. Characterization of 3D-printed scaffolds

Surface topography imaging and elemental analysis of the scaffolds were performed using a field emission scanning electron microscope and energy-dispersive X-ray spectroscopy (SEM-EDS, GEMINISEM 500, Zeiss, Oberkochen, Germany). The porosity of the scaffolds was calculated using the ethanol replacement method [15], according to the following formula:

$$\text{Porosity (\%)} = (V1 - V3) / (V2 - V3) \times 100\%$$

where V1 is the total volume after adding absolute ethanol to the graduated cylinder and immersing the scaffold sample in it. V2 is the total volume recorded after the air in the pores of the material was evacuated by a vacuum desiccator, and the pores were filled with ethanol. V3 is the total volume of the material after the graduated cylinder was removed. The pore connectivity of the scaffolds was calculated using high-resolution micro-CT (Siemens, Munich, Germany) imaging according to the following formula:

$$\text{pore connectivity} = (\text{connected pore volume} / \text{sum of connected and closed pore volumes}) \times 100\%$$

The paste used to print the scaffold was put into a mold and cast into a 1-mm thick film. After the solvent evaporated, it was cut into a 10 mm \times 10 mm-size test sample for Fourier transform infrared (FTIR). The functional groups of the scaffolds were analyzed by FTIR spectroscopy (Nicolet ISS50, Thermo Fisher, MA, USA) using the KBr particle technique at room temperature ranging from 500 to 3000 cm^{-1} . The mechanical properties of the scaffolds (10 mm \times 10 mm \times 4 mm) were tested. A dynamic material testing machine (AGS-X 5 KN, SHIMADZU, Kyoto,

Japan) was used to assess a loading pressure of 250 N (N) at a speed of 1 mm/min. Three samples in each group were tested to obtain the load-displacement curve, and Young's modulus and compressive strength of the support also were calculated. The scaffold (10 mm × 10 mm × 4 mm) was immersed in a centrifuge tube containing 10 mL PBS under a constant temperature incubator shaker at 37 °C for 1, 4, and 7 days and 2, 4, 6, 8, 10, and 12 weeks. The degradation solution was collected at each time point. The concentrations of Ca²⁺ and Zn²⁺ in the solution were measured by inductively coupled plasma emission spectrometry (iCAP6300, Thermo Fisher, MA, USA).

2.3. In vitro cell experiments

2.3.1. Cytocompatibility test

Rat BMSCs (Cyagen Biosciences, CA, USA) were used to study the effects of the scaffold (5 mm × 5 mm × 2 mm) on cell viability, adhesion and proliferation. The BMSCs were cultured in Dulbecco's Modified Eagle Medium (DMEM, Gibco, MA, USA) with 10% fetal bovine serum (FBS, Gibco, MA, USA) and 1% penicillin-streptomycin (PS, Gibco, MA, USA) at 37 °C and 5% CO₂. The scaffolds were presoaked in a medium processed in 48-well cell culture plates. The BMSCs were then seeded on the scaffolds in well plates at a density of 2 × 10⁴ cells/well. After 7 days of culture, the cells were stained using a live/dead cell assay kit (Thermo Fisher, MA, USA) for 15 min. Living cells (green) and dead cells (red) were observed under a fluorescence microscope (Axio Imager. d2, ZEISS, Oberkochen, Germany), and cell viability was analyzed. Cell morphology was also observed after 7 days of culture. Cells were washed 3 times with PBS, fixed with 4% paraformaldehyde solution for 10 min, soaked with 0.2% Triton X-100 for 15 min, and then washed with PBS. Fluorescein isothiocyanate (FITC, Sigma, MA, USA)-phalloidin and 4,6-Diamidino-2-phenylindole dihydrochloride (DAPI, Sigma, MA, USA) were stained for 30 min and 5 min, respectively, to label the actin and nuclei of the cells. The cell morphology on the scaffold was then observed by laser scanning confocal microscopy (LSCM, ECLIPSE Ti2, Nikon, Tokyo, Japan). Cell proliferation was analyzed using a Cell Counting Kit-8 (CCK-8, Dojindo, Kumamoto, Japan). After 1, 4, and 7 days of culture, 200 µl DMEM containing 10% CCK-8 was added to each well in 48-well plates and incubated for 1 h. Then 100 µl of the mixture was transferred to each well in the 96-well plates. The absorbance of the solution was measured at 450 nm using a microplate reader (Synergy-Neo2, Biotek, VA, USA). After 7 days of culture, according to the instructions of Annexin V FITC Apoptosis Detection Kit (Dojindo), the cells were collected and made into a cell suspension with a concentration of more than 1 × 10⁵ cells/ml. Cell apoptosis was detected by flow cytometry (Attune Nxt 3L-BRV, Thermo Fisher, USA). All experiments were performed in triplicate.

2.3.2. Alkaline phosphatase (ALP) activity

The BMSCs were cultured in an osteogenic induction medium on 7th, 14th day and then stained with ALP using a chromogenic kit (Beyotime, Jiangsu, China). The scaffolds were removed before ALP staining to unify the method with ARS staining. Images were taken using a digital camera and a microscope. After 7 and 14 days of culture, the cells were lysed using RIPA lysis buffer (Thermo Fisher, MA, USA), and the proteins were collected. ALP activity was then measured using an ALP detection kit (Beyotime, Jiangsu, China), and then the BCA protein detection kit (Thermo Fisher, MA, USA) was used to detect the total protein concentration for data normalization.

2.3.3. Alizarin red S (ARS) staining

The scaffolds and BMSCs were cultured in an osteogenic induction medium. ARS staining was used to show the mineralized nodules. The scaffolds were removed before ARS staining to exclude the interference of Ca components in the scaffolds on the staining. After 21 days of culture, the BMSCs were fixed with 4% paraformaldehyde solution, washed three times with PBS, and stained with a 2% ARS (Beyotime,

Jiangsu, China) solution. They were incubated at room temperature for 30 min and then washed with distilled water. Images were taken by digital camera and microscope. The mixture was then augmented with 10% acetic acid and incubated overnight. The mixture was then centrifuged at 20,000 g for 15 min to obtain a supernatant that was neutralized with 10% ammonium hydroxide. Then 100 µl/well of the mixture was added to the 96-well plate, and a microplate reader was used to measure the absorbance of the solution at 405 nm for quantitative analysis.

2.3.4. Quantitative real-time PCR (Polymerase Chain Reaction) analysis

Real-time PCR was used to detect mRNA transcription levels of osteogenic specific gene runt-associated transcription factor 2 (Runx2), type I collagen (Col I), osteopontin (OPN), and osteocalcin (OCN). The cells were cocultured with the scaffold at a density of 2 × 10⁵ cells/well in a 6-well cell culture plate. After 14 days of osteogenic induction, total RNA was extracted from the cells using TRizol reagent (Invitrogen, MA, USA). RNA samples were post-reverse-transcribed using Bestar™ qPCR RT Kit (DBI® Bioscience, Germany), Bestar® SybrGreen qPCR Master Mix (DBI® Bioscience, Germany), and real-time PCR (QuantStudio 3, Applied Biosystems, MA, USA). Real-time quantitative PCR detection was then performed with β-actin as a reference. The primer sequences are described in [Supplementary Table S2](#).

2.3.5. Western bolt analysis

The total amount of cellular protein was extracted and quantified after 14 days of osteogenic induction culturing with the scaffolds and BMSCs. The samples were then subjected to SDS electrophoresis and transferred to a polyvinylidene fluoride membrane (0.22 µm, Millipore, MA, USA). After 1 h of sealing with 5% skim milk, the primary antibody was incubated: Runx2 (Abcam, AB236639, 1:1000), Col I (Proteintech, 14695-1-AP, 1:1000), OPN (Proteintech, 22952-1-AP, 1:1000), and OCN (AB clone A6205, 1:2000), and then left overnight at 4 °C. After washing three times with TBST, the cells were incubated with enzyme-linked secondary antibody (EASYBIO, BE0101/BE0102, 1:500). The protein signal was visualized using a chemiluminescence imaging instrument (5200, Tanon, Shanghai, China), and then quantitatively analyzed by Image-J software.

2.3.6. Proteomics analysis

The BMSCs were cocultured osteogenically with the scaffolds for 14 days. Proteins were extracted in 8 M urea and digested using FASP. The tryptic peptides were desalted on C18 cartridges. The elution products were resolved in 0.1% FA with iRT spiked. They were delivered to liquid chromatography (EASY-nLC1000, Thermo Fisher Scientific, MA, USA) coupled with a mass spectrometer (Orbitrap Fusion Lumos, Thermo Fisher Scientific, MA, USA). Peptides were separated by a capillary LC column (75 µm × 100 mm, C18). The eluted duration was 60 min. The data were acquired by data-independent acquisition (DIA) using the following parameters: positive mode was set. One cycle contained one full and 19 segment fragments scans. The full scan range was from 350 to 1300 m/z screened at 120,000 resolutions. Fragment spectra were collected at a resolution of 3000. Raw data were analyzed using Spectronaut (version 14.3, Biognosys, Schlieren, Switzerland). The spectral library was generated using all the raw data files. The search parameters were set to MS and MS/MS tolerances at 10 ppm and 0.02 Da. Two missed cleavages were allowed; the fixed modification was carbamidomethylation, and the SwissProt database was rat-restricted. The samples were quantitatively evaluated based on the MS2 area. Cross runs were normalized according to the global abundance area.

2.3.7. RAW cell polarization

In a 12-well plate, 1 × 10⁵ murine-derived macrophage cells (RAW264.7) were seeded per well. After culturing for 4 days, the cells were digested, centrifuged, and washed with 1% BSA for 0.5 h to block non-specific antigens. Cells were then stained with fluorescent-

conjugated CD68 and CD86 antibodies (eBioscience, USA) as M1 markers and CD206 antibody (eBioscience, USA) as M2 marker for 1 h at room temperature [34]. After washing the cells three times with 1% BSA, 100 μ l of the suspension was aspirated into a 96-well plate for analysis by flow cytometry (LSRFortessa, BD, USA).

2.4. In vivo repair of bone defects by scaffolds

2.4.1. Bone defect model and scaffold implantation

A rat model of a femoral condyle defect was used to study the osteogenic ability of the scaffolds *in vivo*. The animal experiments were approved by the Animal Ethics Committee at Peking Union Medical College Hospital (XHDW-2022-018). Eight-week-old (300–350 g) male Sprague Dawley (SD) rats (Charles River Laboratories, Beijing, China) were injected intraperitoneally with 3% sodium pentobarbital (30 mg/kg body weight) during general anesthesia. The skin and hair were removed and disinfected, and the femoral condyle was cut open to expose it. Then, a cylindrical hole with a diameter of 3 mm and a depth of 3 mm was made using an electric drill, and the temperature was maintained with ice derived from salt water, at all times. The broken bones were removed, and the drilled holes were rinsed. The scaffolds were implanted into the defect and then divided into four experimental groups according to the following implantation conditions: 1. No scaffold implantation group (Control); 2. P scaffold implantation group (P); 3. PLGA/ β -TCP (2:1) scaffold implantation group (PT); 4. PLGA/ β -TCP/Zn (1 wt%) scaffold implantation group (PTZ). Finally, the incision was closed layer by layer with sutures, and antibiotics were administered for 3 days after the surgery.

2.4.2. Radiographical evaluation

The rats were sacrificed at 4th, 8th, and 12th week postoperatively, and the femoral condyles were removed to evaluate new bone formation in the scaffold at the defect using high-resolution Micro-CT (Siemens, Munich, Germany). Scanning was performed with resolution 20 μ m, voltage 60 kV, and current 400 μ A. The mean CT values of new bone and scaffold analyzed by INVEON Workplace software were 3590HU and 1890HU, respectively. Region of interest (ROI) was selected according to the anatomical location of the bone defect. First, the CT value of the new bone tissue was used to identify and select the new bone tissue in the ROI. Then, the scaffold in the ROI was identified and selected by using the CT value of the scaffold. By removing the selected portion of the scaffold from the selected portion of the newly formed bone tissue, the actual portion of the newly formed bone tissue in the scaffold could be obtained. Statistical analysis was performed on the bone tissue volume/total tissue volume (BV/TV), trabecular number (Tb-N), trabecular separation/spacing (Tb.Sp) of new bone tissue in each group.

2.4.3. Histological and immunohistochemical analysis

Femur samples were decalcified by 10% EDTA (Beyotime, Jiangsu, China) at 37 °C for 8 weeks. After decalcification, the paraffin-embedded femoral tissue (about 2 mm in thickness) containing the bone defect was cut into serial sections 3 μ m thick. The sections were routinely histologically stained by hematoxylin and eosin (H&E) and Sirius red (SR, Beyotime, Jiangsu, China). Immunohistochemical staining of osteogenesis-related markers BMP2 (Proteintech, 66,383-1-ig), OPN (Proteintech, 22952-1-AP), anti-inflammatory marker IL-10 (Proteintech, 60,269-1-ig) and pro-inflammatory marker TNF- α (Proteintech, 60,291-1-ig) were performed to assess the expression of proteins associated with osteogenesis and inflammatory responses in the implanted scaffold area. Signal intensities were quantified using Image-J software. All tests were repeated in three specimens. The immunohistochemical experiments were performed in parallel using the same concentration of nonspecific immunoglobulin from the same species as the isotype control. The results are shown in Supplementary Fig. S4.

2.5. Statistical analysis

All quantitative data in the experiments were presented as means \pm standard deviations (SD). The each two groups of data were compared using the Student's *t*-test. A value of $p < 0.05$ was considered statistically significant. The statistical analysis and graphing were performed using GraphPad Prism software (GraphPad Software Inc, CA, USA).

3. Results

3.1. Effects of the scaffolds on the cytocompatibility of BMSCs and screening of the composition ratios of the scaffolds

The size of the scaffold used in cell experiments was 5 mm \times 5 mm \times 2 mm (Fig. 1a). We first evaluated the cell proliferation ability of scaffolds in different ratios of PLGA and β -TCP (w/w of 4:1, 3:1, 2:1), and found that the proliferation ability of PLGA/ β -TCP scaffolds was better when the ratio was 2:1 (Fig. 1b). Additionally, that previous studies have confirmed the osteogenic effect by adding 0.65–5 wt% Zn to polymers [24,27,35–38]. On this basis, we explored the non-toxic Zn addition content in the following experiment. Therefore, we further added different ratios (1 wt%, 2 wt%, 3 wt%, 4 wt%) of Zn-SPs into the PLGA/ β -TCP (2:1, PT) scaffold. The results showed that PLGA/ β -TCP/Zn (Zn-SPs content of 1 wt%, PTZ) scaffolds had a high cell proliferation rate than the other group, and cell proliferation of the other three groups almost unchanged at 1st, 4th, 7th day (Fig. 1c). Furthermore, the PTZ group has a low apoptosis ratio and dead cell ratio of 15.184 \pm 3.436% and 3%, respectively. However, in the other three group (Zn-SPs content of 2 wt%, 3 wt%, 4 wt%), the apoptosis ratios and dead cell ratios were 74.667 \pm 2.901%, 74.833 \pm 4.500%, 74.667 \pm 3.083% and 88.220 \pm 0.078%, 94.308 \pm 0.710%, 97.001 \pm 0.620%, respectively (Fig. 1d, e, g and h). It indicated that the scaffolds have obvious cytotoxicity when the Zn-SPs exceeded 2 wt%, and the higher the content of Zn-SPs the more obvious cytotoxicity was found. Meanwhile, we found that the ratio of viable and apoptotic cells on P and PT scaffolds was not significantly different from that of PTZ scaffolds, which also had good cytocompatibility. BMSCs were also found attached well on P, PT and PTZ scaffolds, and the antennae of BMSCs in PTZ group were distributed and extended more widely than P and PT groups (Fig. 1f). Therefore, we will further study the P, PT and PTZ scaffolds to verify the changes in the osteogenesis and anti-inflammatory capabilities after adding Zn-SPs.

3.2. Analysis of the structure, composition, mechanical properties and Ca^{2+}/Zn^{2+} release of the scaffolds

There were no significant differences in size, pore size, porosity and connectivity among P, PT and PTZ printed by 3D LT-RP. The dimensions of the printed scaffolds were 10 mm \times 10 mm \times 2 mm (Fig. 1a), with pore diameters ranging 506.6–531.3 μ m and porosities ranging 66.4%–68.2% (Fig. 2a, Fig. S1, Table 1). The top and side views of the pore structure inside the scaffold showed that all pores were interconnected with 100% connectivity (Fig. 2b). The SEM results showed that the microporous structures on the surface of the three scaffolds were different (Fig. 2c). The surface of P was rich in microporous structures with pore sizes ranging 0–20 μ m. In PT scaffold, the β -TCP particles were uniformly dispersed in the PLGA matrix, forming a much smaller surface pore structure ranging 0–10 μ m, while a small amount of particle aggregation was observed on the surface of PT scaffold. Whereas the addition of Zn-SPs formed a more finer pore structure with pore sizes of 0–6 μ m in the PTZ scaffold, especially some micropores were below 1 μ m, while less particle aggregation was observed on PTZ scaffold.

We also found that the elements distribution of three groups of scaffolds was approximately the same and dispersed uniformly. The distributions of O and C elements in the three scaffolds, as well as Ca and P elements in the PT and PTZ scaffolds, were similar (Fig. S2). The added Zn elements were scattered along the contour of the PTZ scaffold

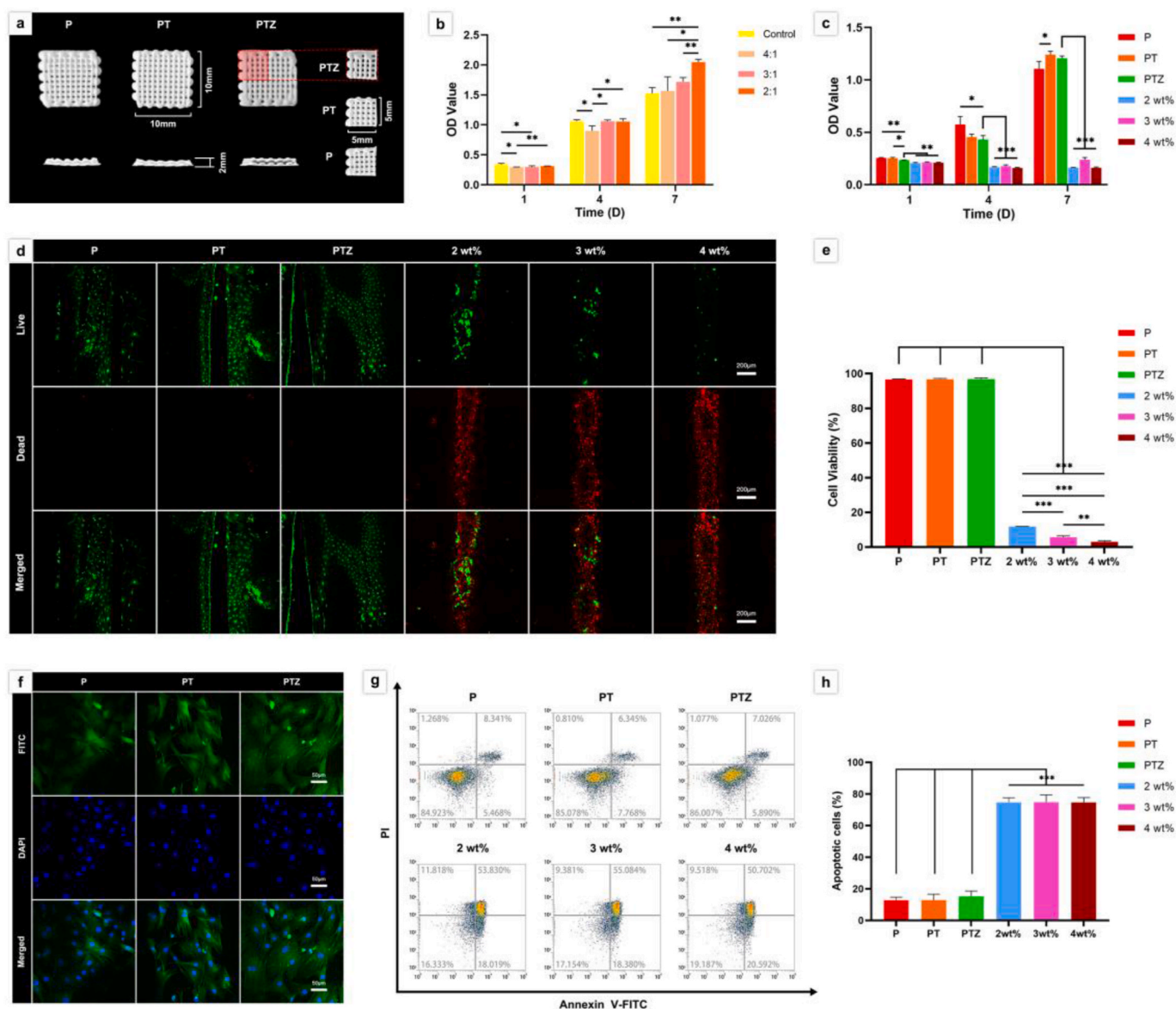


Fig. 1. The macrostructure of scaffolds and the cytocompatibility studies of scaffolds *in vitro*. a. Top view (top line) and side view (bottom line) of LT-RP 3D printed P, PT, and PTZ scaffolds (10 mm × 10 mm × 2 mm), the scaffolds were cut into 5 mm × 5 mm × 2 mm (right) in the cell experiments. b. The effect of well plate and scaffolds with different ratios of PLGA and β -TCP (w/w of 4:1, 3:1, 2:1) on the proliferation of BMSCs. (* $p < 0.05$, ** $p < 0.01$, *** $p < 0.001$ by Student's t-test, $n = 3$). c. The effects of P, PT, PTZ and PLGA/ β -TCP/Zn (Zn-SPs content of 2 wt%, 3 wt%, and 4 wt%) scaffolds on the proliferation of BMSCs. d. Live/dead cells on P, PT, PTZ and PLGA/ β -TCP/Zn (Zn-SPs content of 2 wt%, 3 wt%, and 4 wt%) scaffolds was detected by live/dead assay after 7 days of culture. Live cells with esterase activity appeared green, whereas dead cells with compromised plasma membranes appeared red. The bottom image was merged with the two top images. Scale bar, 200 μ m. e. Quantitative analysis of cell viability on all scaffolds. f. Cytoskeleton (green, FITC-phalloidin) and nuclei (blue, DAPI) were imaged by confocal microscopy after 7 days of culture. Scale bar, 50 μ m. g. Dot plot of Annexin V-FITC/PI of BMSCs in six groups. h. Quantitative analysis of apoptotic cells in six groups.

(Fig. 2d). In addition, the presence of PLGA matrix and β -TCP particles in the scaffolds could be supported by FTIR (Fig. 2e). The presence of four absorption peaks (1181.67, 1746.71, 1081.39, 1267.97) suggested the presence of esters in the PTZ composites. The appearance of three absorption peaks (2851.24, 2946.7, 1381.75) suggested the presence of methyl groups in the material. And esters and methyl groups are the main groups of PLGA matrix. The presence of three other absorption peaks (561.18, 602.65, 1043.3) proved the presence of phosphate, indicating that β -TCP particles were successfully incorporated into the PLGA matrix. The addition of Zn-SPs showed no new characteristic peaks in the FTIR curves, indicating that Zn-SPs did not chemically react with PLGA or β -TCP. The stress-strain curves were obtained from the mechanical tests (Fig. S3), we also found that the compressive strength of the scaffold was improved after the addition of Zn-SPs. The

compressive strength of the PTZ scaffold (2.887 ± 0.025 MPa) was higher than that of PT scaffold (2.563 ± 0.103 MPa) (Fig. 2g). However, there was no significant difference of the Young's modulus between PTZ (63.41 ± 1.89 MPa) and PT scaffold (60.41 ± 0.74 MPa) (Fig. 2f).

The release of Ca^{2+} from PT, PTZ and Zn^{2+} from PTZ was detected by soaking the scaffolds in PBS for various time. The Ca^{2+} was produced by the degradation of β -TCP in PT and PTZ scaffolds, whereas Zn^{2+} was produced by the degradation of Zn-SPs. The cumulative release curves of Ca^{2+} and Zn^{2+} were observed for 16 weeks (Fig. 2h). During the first 14 days of degradation, a steady rise of Ca^{2+} concentration in PTZ scaffolds was observed, from 0.187 ± 0.055 $\mu\text{g}/\text{mL}$ at 1 day to 1.331 ± 0.251 $\mu\text{g}/\text{mL}$ at 14th day. This steady increase of the Ca^{2+} continued until 16th week, with the concentration reached 13.244 ± 0.626 $\mu\text{g}/\text{mL}$, and the increased releasing trend indicated that the Ca^{2+} concentration would

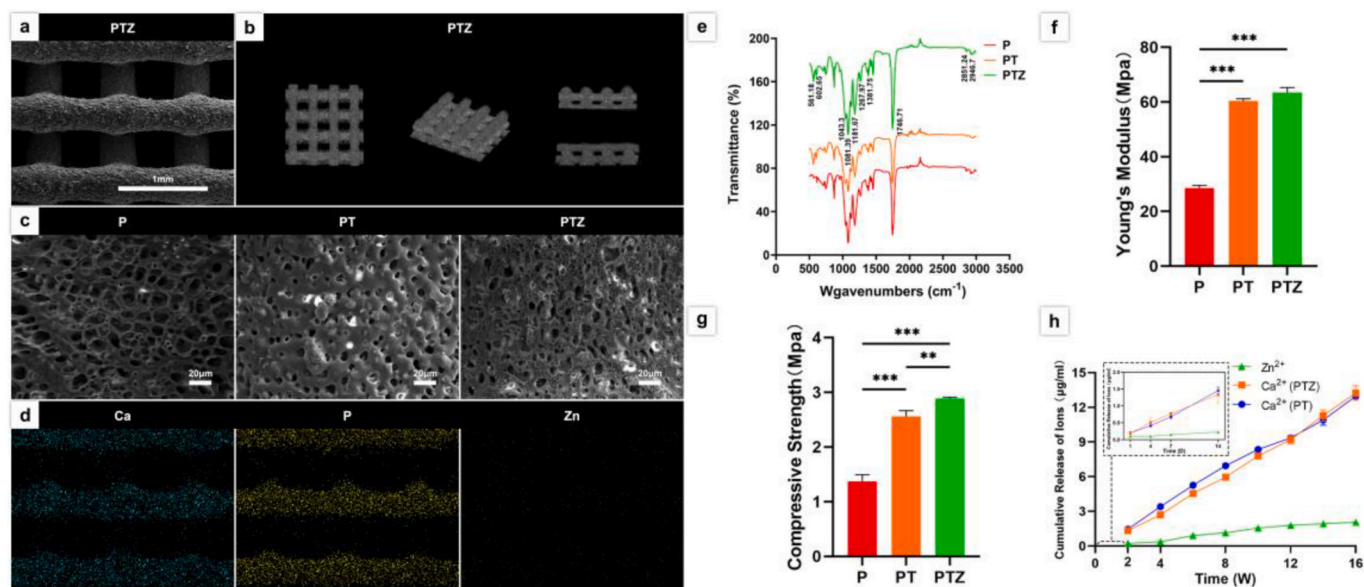


Fig. 2. Characterization of the scaffolds. a. SEM images of the surface topography of PTZ scaffolds. b. Micro-CT images of the internal pore connectivity of PTZ scaffolds. c. SEM images of the surface topography of the three groups of scaffolds. d. Ca (blue), P (yellow) and Zn element (green) analysis of PTZ scaffold using SEM-EDS. e. FTIR analysis of functional groups in three scaffolds. f. Stress-strain curves of the three scaffolds. f. The Young's modulus of three scaffolds. g. The compressive strength of three scaffolds. h. Cumulative release of Ca^{2+} from PT, PTZ scaffolds and Zn^{2+} from PTZ scaffolds within 16 weeks *in vitro*.

Table 1

Macropore size, porosity and internal pore connectivity of scaffolds.

Group (n = 3)	P	PT	PTZ
Macropore size (μm)	506.6 ± 18.2	531.3 ± 28.5	515.7 ± 15.2
Porosity (%)	68.2 ± 2.8	67.1 ± 3.2	66.4 ± 5.3
Internal pore connectivity (%)	100	100	100

continue to rise afterwards. The released Ca^{2+} in PTZ was similar to that of PT scaffolds, indicating that the addition of Zn-SPs have no significantly effect on the release of Ca^{2+} . However, Zn^{2+} was released slowly during the first 7 days, and the concentration was only $0.149 \pm 0.021 \mu\text{g/mL}$ at 7th day. After 7 days, Zn^{2+} was gradually and steadily released over time and continued until 12th week, reaching a concentration of $1.792 \pm 0.201 \mu\text{g/mL}$. However, the release of Zn^{2+} was gradually plateaued until 16th week with the concentration of $2.055 \pm 0.223 \mu\text{g/mL}$, and the accumulated release ratio of Zn was 48.2% at 16th week in PTZ scaffold.

3.3. Osteogenic differentiation of BMSCs with scaffolds

By ALP and ARS staining, we observed the effects of PTZ scaffolds on osteogenic activity and osteomineralization of BMSCs, respectively. After the addition of Zn-SPs, the ALP activity of BMSCs in PTZ group was higher than PT group, and this increased activity was more pronounced at 7th day and lasted until 14th day (Fig. 3a). The PT group showed more calcium deposition than the P group, and the density of calcium deposition in PTZ group was higher than PT group (Fig. 3b).

To further confirm the osteogenic differentiation ability of PTZ scaffold, we also examined the expression of osteogenic genes and proteins at specific time points using RT-qPCR and WB techniques. Osteogenic differentiation markers such as Runx2, Col I, OPN and OCN were detected, and β -actin was used as a reference. The results showed that the addition of Zn-SPs caused an increase in OPN and OCN gene expression during the first 7 days (Fig. 3c). At 14th day, Runx2, Col I and OPN gene expressions were higher in PTZ group than PT group (Fig. 3c), and Runx2, Col I and OCN protein expressions were also higher than PT group (Fig. 3d). The up-regulation of osteogenic gene and protein

expression suggested the enhancement of osteogenic differentiation ability after the addition of Zn-SPs. Changes in gene and protein expression at different time points might be related to the period in which they performed their functions.

We further investigated the molecular mechanism of how does Zn-SPs promote osteogenic differentiation of BMSCs. We performed proteomic analysis using the Ingenuity Pathway Analysis (IPA) platform, as shown in Fig. 4a. The volcano map of all detected and expressed proteins showed a total of 5169 proteins, and the differentially expressed protein clusters showed 43 proteins upregulated and 28 proteins downregulated in PTZ group compared to the PT group. Based on the analysis of known proteins, 25 proteins related to osteogenesis were screened out (Fig. 4b). The heat map showed that the expression of proteins favoring osteogenic differentiation were upregulated in PTZ group compared to PT group, while the expression of proteins related to inhibition of osteogenic differentiation and pro-inflammation were lower than that of the PT group (Fig. 4b). The network diagram (Fig. 4c) also listed the protein interactions and expressions that favored the osteogenic process. The results showed that the addition of Zn-SPs upregulated the expression of osteogenic proteins and suppressed the expression of proteins that unfavorable to osteogenesis. Our further analysis revealed that several proteins (BCL9L, FZD2, ENPP1, HTRA1, CACNA2D1, CADM4 and RDH16) had direct or indirect effects on the expression of CTNNB1 protein (β -catenin). Among them, the expression of BCL9L, FZD2, ENPP1 and HTRA1, which directly affected β -catenin, was upregulated (Fig. 4d).

3.4. Anti-inflammatory effect of scaffolds on cells *in vitro*

We also noted changes in anti-inflammatory and pro-inflammatory protein expression using proteomic analysis (Fig. 4b). The heat map showed that the expression of anti-inflammatory-related proteins was upregulated in PTZ group compared to PT group, and the expression of pro-inflammatory-related proteins was lower than PT group, suggesting that the addition of Zn-SPs may have equipped the scaffold with an anti-inflammatory effect. To verify the existence of anti-inflammatory effect, we investigated the macrophage polarization affected by PTZ scaffold. The results showed that the percentage of macrophages with M1 phenotype decreased and the percentage of M2 phenotype increased in

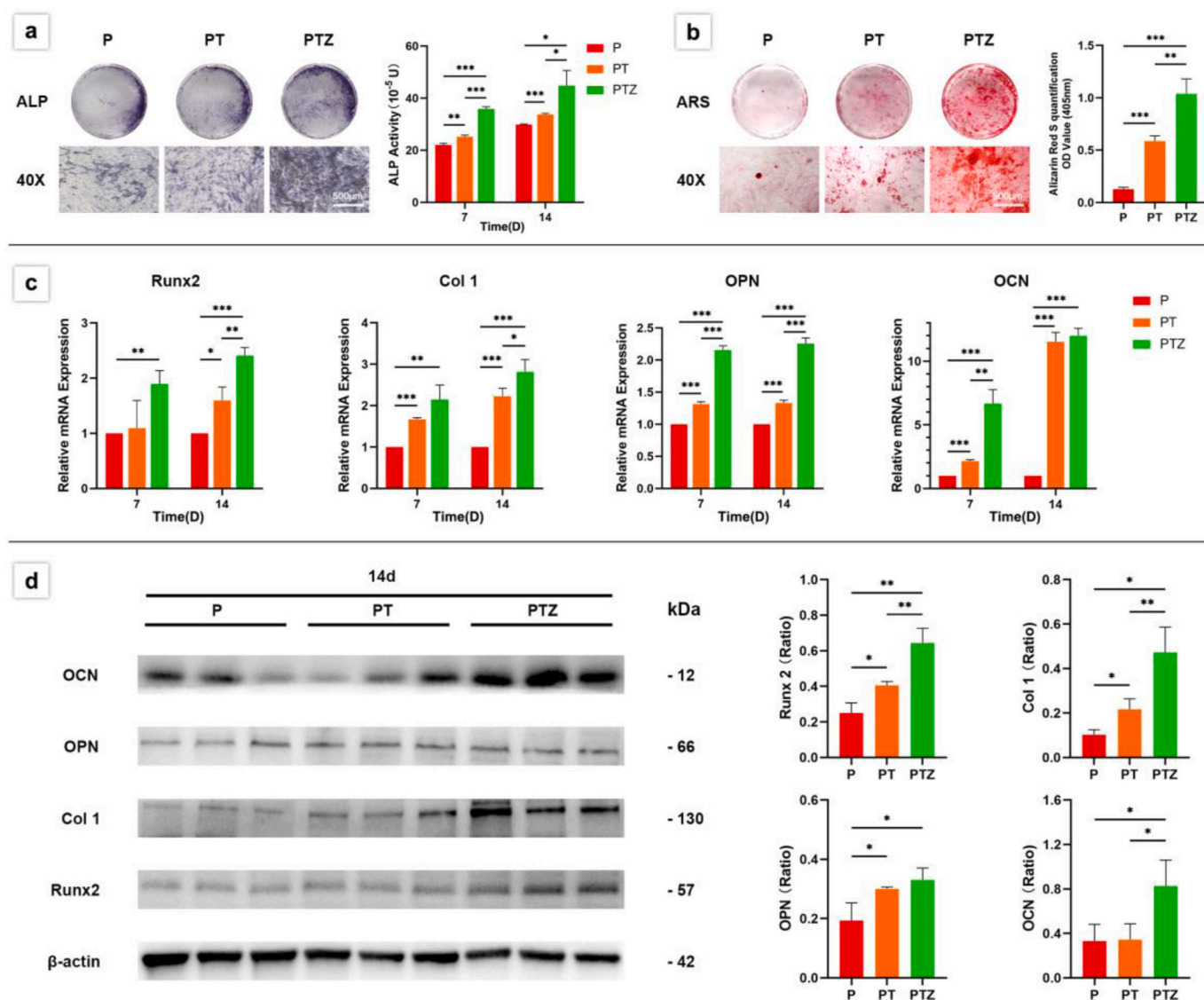


Fig. 3. Osteogenic differentiation ability of BMSCs co-cultured with three groups of scaffolds. a. A quantitative analysis was performed after ALP staining at 7th and 14th day. b. Calcium deposits were stained with alizarin red S and quantitatively analyzed after 21 days of culture. c. The expression levels of Runx2, Col I, OPN and OCN were analyzed by RT-qPCR after 7 and 14 days. d. The expression levels and quantitative analysis of Runx2, Col I, OPN, and OCN proteins detected by WB after 14 days. β -Actin was used as a protein loading control.

PTZ group compared with PT group (Fig. 4h), indicating that the addition of Zn-SPs prompted the conversion of macrophages from M1 phenotype to M2 phenotype. To further investigate the mechanism by which this anti-inflammatory effect occurs. We further performed a predictive analysis of cellular pathways using IPA software (Fig. 4e). The upregulation of the anti-inflammatory protein CCN2 and the downregulation of the pro-inflammatory proteins IL1RN and EIF2AK2 indicated the activation of the P38 MAPK pathway as well as the inhibition of the NF κ B pathway. Moreover, through changes in the expression of multiple proteins, we also found that the expression of the pro-inflammatory protein TNF was downregulated (Fig. 4g). The above results showed that the scaffold could promote anti-inflammatory response and inhibit pro-inflammatory response.

3.5. Radiographical evaluation of bone regeneration

A cylindrical structure with diameter and depth of 3 mm (Fig. 5a) was printed for *in vivo* experiments. A rat femoral condyle defect with diameter and depth of 3 mm was constructed firstly, and the implanted

scaffolds could fill the bone defect well (Fig. 5b). Fig. 5c showed the micro-CT 3D reconstructed images of the new bone tissue in the rat femoral condyle defect at 4th, 8th, and 12th week after surgery. In the 4th week after surgery, the amount of new bone in each group was low. The bone regeneration rate of PTZ scaffold was faster than the other groups, and new bone was observed along the outline of the scaffold. At 8th week after surgery, the formed new bone in PT and PTZ groups have passed through the transverse diameter of the scaffold. At 12th week after the surgery, the amount of new bone increased than the 8th week in PT and PTZ groups. The new bone not only covered the bottom surface of the bone defect, but also grew to a certain depth along the scaffold.

We performed a quantitative analysis of the 3D reconstructed new bone tissue (Fig. 5d–f). We found that at 4th, 8th and 12th week post-operatively, Tb-N in PTZ group was always higher than PT group while Tb.Sp was always lower than PT group, indicating that the amount of new bone was high and dense in PTZ group. In contrast, the BV/TV value in PTZ group has nosignificantly difference with that in PT group at 4th week, but were higher than those in PT group at 8th and 12th week,

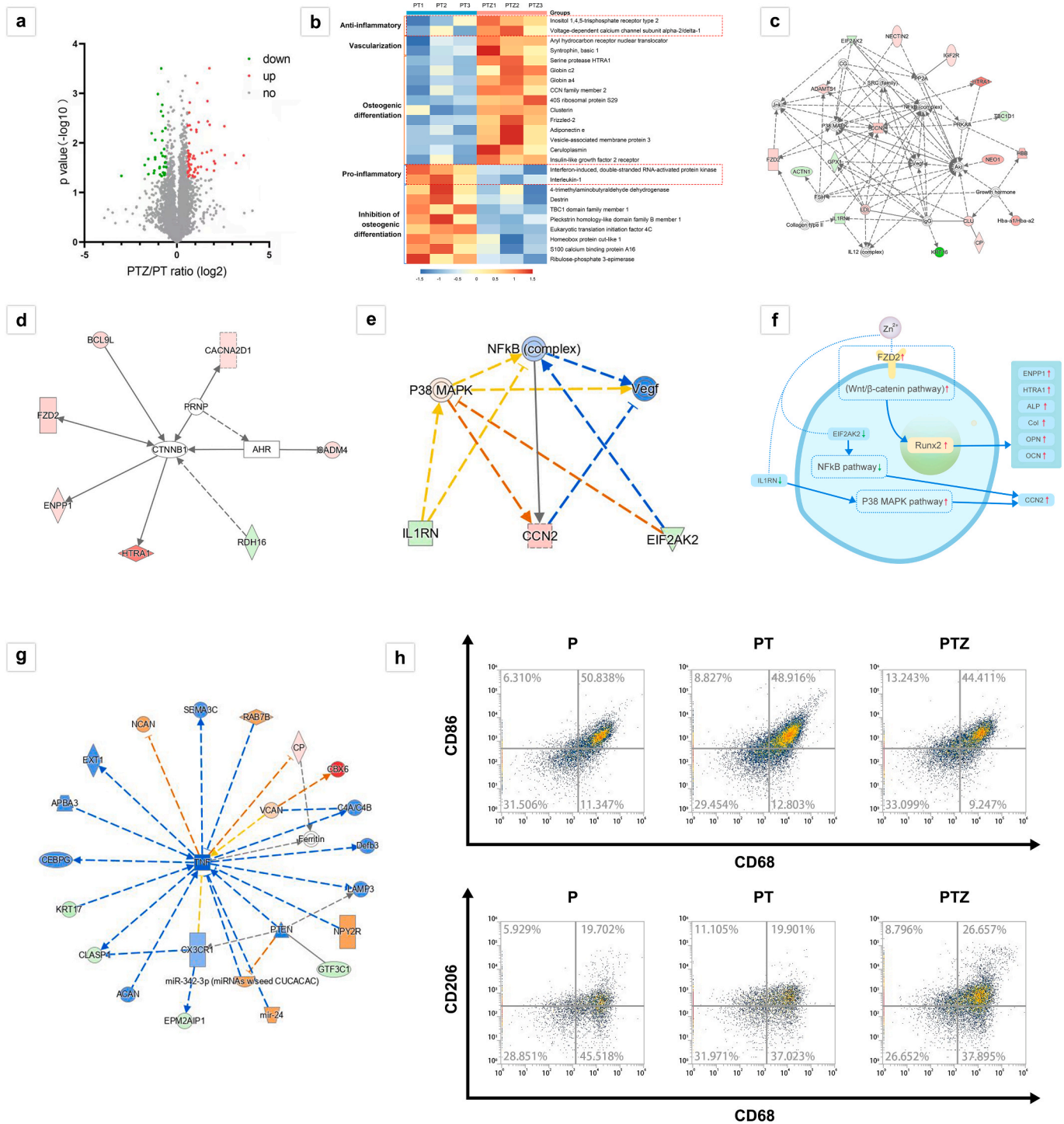


Fig. 4. Protein expression and bioinformatics analysis of BMSCs with PT and PTZ scaffolds. a. Volcano plot of differentially expressed proteins between PT and PTZ groups. (1.5-fold change; red: upregulated proteins; green: downregulated proteins). b. Heat map of osteogenesis related protein expression (red dotted box marked the expression of anti-inflammatory and pro-inflammatory related proteins). c. Network diagram showing the connections between osteogenesis related proteins. d. The expression of various proteins (BCL9L, FZD2, ENPP1, HTRA1, CACNA2D1, CADM4, and RDH16) that directly or indirectly affect the expression of CTNNB1 protein. e. The expression level of anti-inflammatory protein (CCN2) and pro-inflammatory proteins (IL1RN and EIF2AK2) and related cellular pathway prediction analysis (orange: activation; blue: inhibition; yellow: unpredictable). f. Schematic diagram of the molecular mechanism of PTZ group to promote osteogenic differentiation and produce anti-inflammatory effects in cells. g. Expression prediction map of pro-inflammatory protein TNF and its expression-related proteins. h. Flow cytometry results of surface marker CD68, CD86 and CD206 of polarized RAW264.7 cells in three groups.

indicating that the new bone grew faster after 4 weeks in PTZ group.

3.6. Histological and immunohistochemical analysis of bone regeneration

The formation of new bone were reconfirmed by histological

analysis. At 4th week postoperatively, the formation of new bone was not visible in four groups, but new fibrous tissue (red arrows) appeared in control and P groups (Fig. 6b). And osteoblasts (purple arrows) appeared in PTZ group at 4th week (Fig. 6a). The amount of new bone (blue arrows) was higher in PTZ group than PT group at 8th and 12th

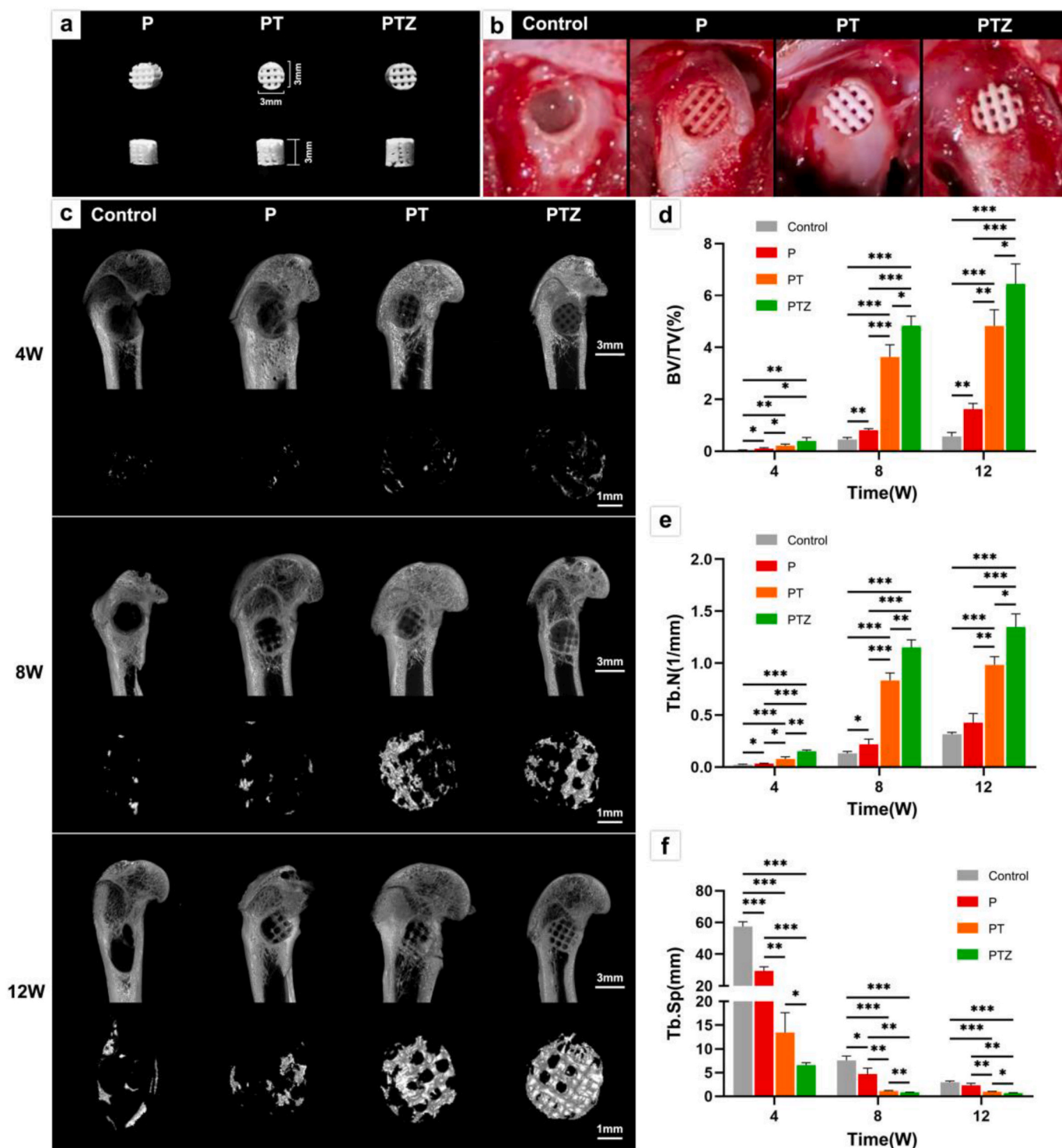


Fig. 5. Animal experiments and micro-CT analysis of bone regeneration. a. Top view (top) and side view (bottom) of the P, PT, and PTZ scaffolds (D = 3 mm, H = 3 mm) used in the animal experiments. b. Images of the surgical area without scaffold implantation (control group) and after implantation of three groups of scaffolds. c. Representative micro-CT 3D images of the region of interest (ROI) in the femoral condyle defect area at 4th, 8th and 12th week post-surgery. Scale bar, 3 mm and 1 mm. Quantitative analysis of BV/TV (d), Tb.N (e) and Tb. Sp (f) of the new trabecular bone in the bone defect area at 4th, 8th and 12th week after surgery (control group shown in gray).

week (Fig. 6a). At 12th week postoperatively, a small amount of new bone was also observed in the control and P groups, while more fibrous tissue was seen to be encapsulated. In contrast, PTZ group had less new fibrous tissue than the other three groups and residual scaffolds (black arrows) could be seen in some sections (Fig. 6b).

To further clarify the mechanism of PTZ scaffolds in promoting bone

regeneration, we applied immunohistochemical staining and quantitative analysis to detect the expression levels of BMP2, OPN, IL-10 and TNF- α in tissues (Fig. 7). We performed nonspecific immunohistochemical isotype control staining to ensure that the staining was specifically binding firstly (Fig. S4). We found that BMP2 and OPN were significantly expressed at 4th week in PTZ group, and the expression

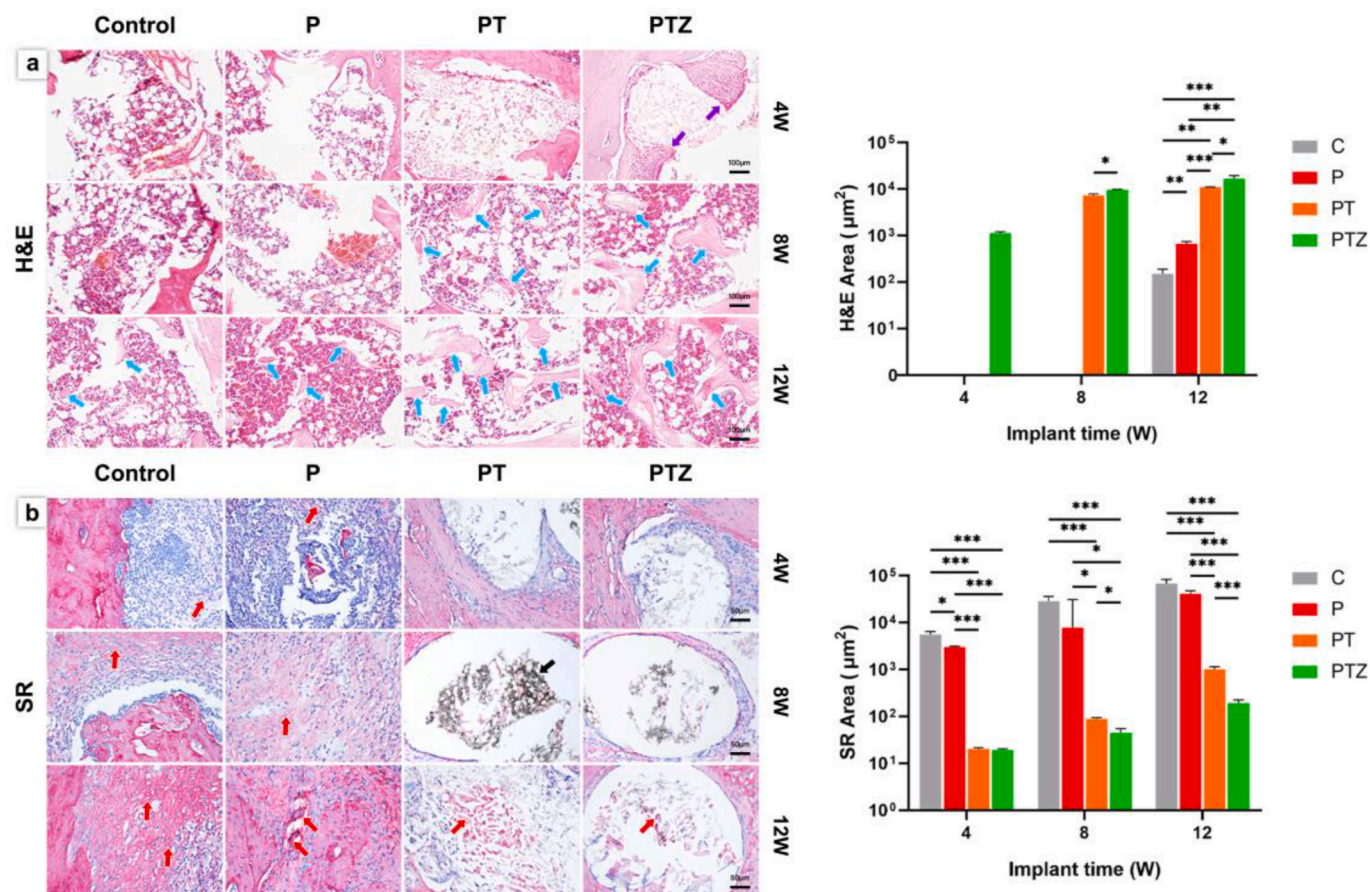


Fig. 6. Histological images and quantitative analysis of new bone after scaffold implantation. a. H&E staining image of decalcified tissue section under a 100 × microscope; purple arrows showed osteoblasts; blue arrows showed new bone tissue. Scale bar, 100 µm. b. Sirius red staining images and quantitative analysis of decalcified tissue section under a 200 × microscope; red arrows showed new fibrous tissue; black arrows showed scaffold. Scale bar, 50 µm.

levels were gradually increased over time until 12 weeks. Regarding to the inflammatory response, the expression of IL-10 was significantly higher and TNF- α was significantly lower in PTZ groups than the other three groups within 12 weeks after implantation.

4. Discussion

Previous studies have confirmed that PLGA/ β -TCP scaffolds have good biocompatibility in animals and humans [27,39,40]. PLGA/ β -TCP at a ratio of 2:1 showed the best effect on the proliferation of BMSCs compared with the ratio of 4:1 and 3:1. Also, it has been shown that the addition of Mg and Zn can improve the mechanical and osteoinductive properties of PLGA/ β -TCP composite scaffolds [15,27]. However, the problem of the rapid degradation of Mg makes Zn a more suitable metal for degradable bone grafts. But one limitation of Zn containing scaffold is the toxicity caused by excess Zn²⁺ [41,42]. Therefore, we first screened out that the Zn content of 1 wt% was non-toxic, and once Zn content exceeded 2 wt%, the released Zn²⁺ produced obvious toxicity. Meanwhile, PTZ scaffolds continued to release Zn²⁺ for 16 weeks and remained at 2.055 ± 0.223 µg/mL, which below the critical toxic concentration (8.45 µg/mL) [43]. This controlled release of Zn²⁺ could kept Zn²⁺ at a low concentration and reduce the toxicity, which is crucial for the safe application of PTZ scaffolds to humans in the future.

In terms of the structure of scaffolds, the internal pores were connected, and the large pore size was about 500 µm and the porosity was ranging from 60 to 70%, which are favorable for osteogenesis [33,44]. At the same time, it was observed that after adding Zn-SPs, many micropores with the diameter under 1 µm were generated. This multi-level

pore structure and porosity are similar to native cancellous bone [45], and are favorable for BMSCs ingrowth, proliferation, and osteogenic differentiation [46,47]. In terms of composition, the PTZ scaffold contained Ca, P and Zn elements, while demonstrating the successful mixing of PLGA matrix and β -TCP, and the uniformly dispersed Zn SPs in PTZ scaffold. From the FTIR results we can find that Zn-SPs did not chemically react with PLGA or β -TCP, and no characteristic peaks were detected. However, the scattered distribution of Zn-SPs in PTZ facilitated a continuous and stable release of Zn²⁺ from the scaffold during degradation, leading to a long time efficient osteogenesis.

The printed fibers of the scaffolds were spaced vertically and horizontally, and this arrangement (I0°) has been shown to improve mechanics more than other arrangement angles (I10°, I20°, IC30°, I40°, I45°) [48]. Besides that, the agglomeration of β -TCP particles was observed on the surface of the PT scaffold, which was not conducive to the mechanical properties of the scaffold [49]. However, after Zn-SPs added, this agglomeration phenomenon was reduced, possibly because Zn-SPs filled the voids between β -TCP particles, and further improving compressive strength of the scaffold. The Young's modulus and improved compressive strength of PTZ scaffold are close to cancellous bone (Young's modulus: 0.05–0.5 GPA, compressive strength: 0.1–16 MPa) [50], which is beneficial for its future application in orthopedic treatment. Besides, the addition amount of Zn-SPs was limited since the threshold concentration of Zn²⁺ (8.45 µg/mL) was much lower than that of Mg²⁺ (2 mg/mL) [51]. And high Mg containing scaffold may lead to excessive loss of mechanical properties due to hydrogen production in the progress of degradation *in vivo*. The degradation rate of Zn in the human body is more moderate than Mg, which can match the rate of

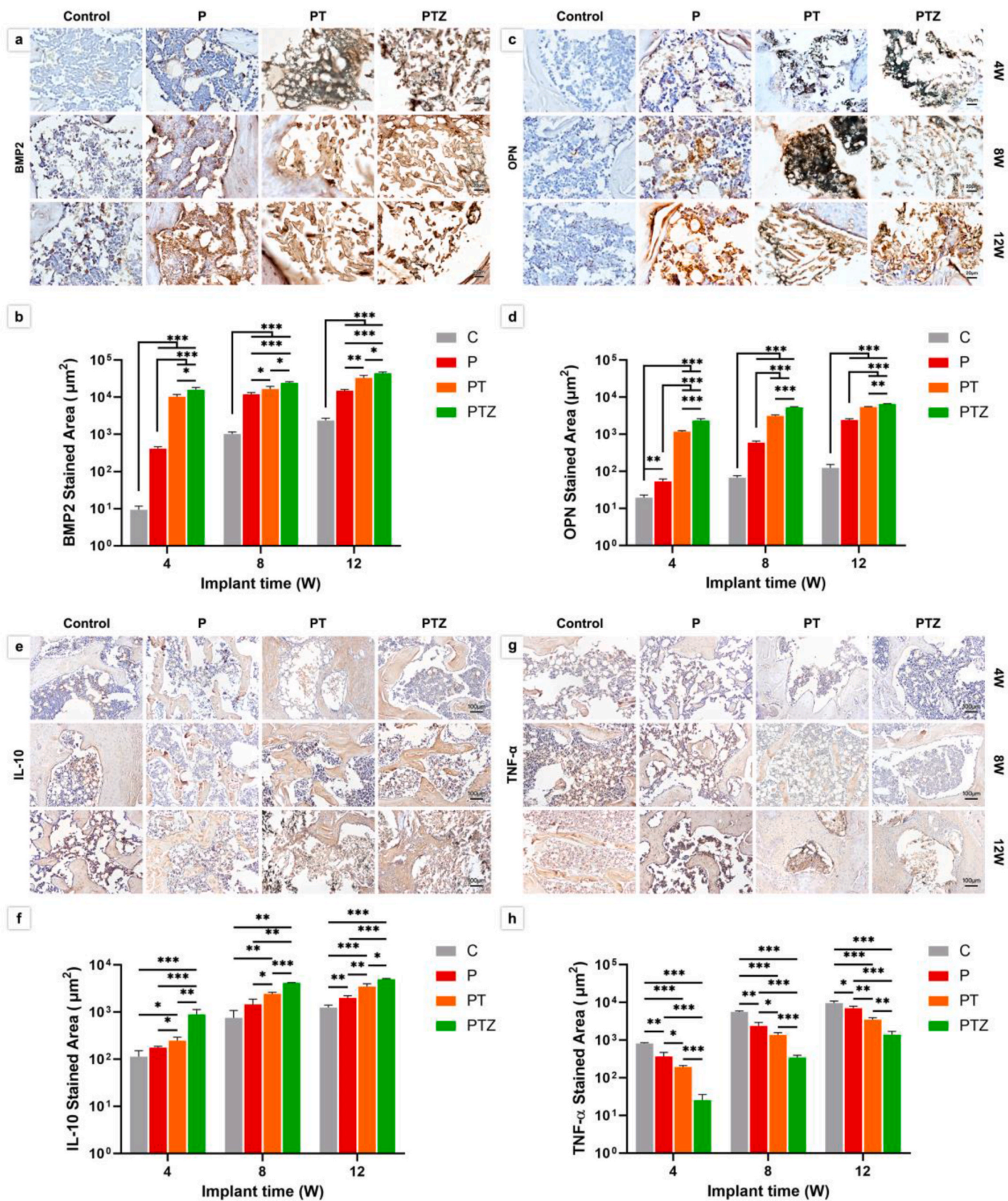


Fig. 7. Immunohistochemical analysis of new bone formation after scaffold implantation. a-d. Expression level and quantitative analysis of BMP2 and OPN after scaffold implantation for 4, 8, and 12 weeks. Scale bar, 20 μm . e-h. Expression level and quantitative analysis of IL-10 and TNF- α after scaffold implantation for 4, 8, and 12 weeks. Scale bar, 100 μm .

bone regeneration [52]. However, the mechanical properties of PTZ should be further improved in the future since they are not fully meet the needs of bone defect regeneration.

Next, the proliferation, adhesion and osteogenic differentiation of BMSCs cultured with scaffolds were verified. The addition of Zn-SPs did not adversely affect the proliferation of BMSCs. Interestingly, the proliferation of BMSCs may be affected by the 20 μm microporous structure on the scaffold surface in the early stage [53], and the proliferation was fast. However, with the continuous release of Ca^{2+} from the scaffold, the proliferation rate of BMSCs was further enhanced. While PTZ scaffold was more favorable for the adhesion of BMSCs. This may be because the early release of Zn^{2+} promotes the adhesion of BMSCs. The improved adhesion property is beneficial to the osseointegration in the early stage of osteogenesis [54], which provides a basis for the subsequent osteogenic differentiation of BMSCs. Subsequently, we investigated the effect of scaffolds on the osteogenic differentiation of BMSCs, the addition of Zn-SPs enhanced the osteoinductivity and promoted the osteogenic activity and mineralization process of BMSCs.

Given that there are lacking of mechanism research on Zn-containing biomaterials promoting bone repair, hence the expression of osteogenesis-related genes and proteins in different stages of osteogenesis was analyzed to explore the potential molecular mechanism of PTZ scaffold. Runx2 is a key osteogenesis specific transcription factor and is considered an early marker of osteogenic differentiation. Col I and OPN are considered to be markers associated with osteogenic mineralization, while OCN is considered to be a late marker of osteogenic differentiation [55]. The addition of Zn-SPs have up-regulation effect on the expression of osteogenic related genes and proteins at earlier stage. As time progressed, the scaffolds without Zn-SPs only up-regulated the expression of Runx2, Col I, OPN and OCN at the gene level, while the scaffolds with Zn-SPs up-regulated the expression at protein level as well. These indicated that the scaffold had little effect on the osteogenic differentiation of BMSCs without the addition of Zn-SPs, and the BMSCs were in the early stage of osteogenesis. The addition of Zn-SPs can accelerate the osteogenic differentiation process.

However, the mechanism by which Zn-SPs trigger the osteogenic differentiation and mineralization process of BMSCs remains unclear. It has been pointed out that particles with a size of 30–150 nm are more favorable for endocytosis, but the particle size of Zn-SPs in this study was 400 nm, which is not conducive to endocytosis. Therefore, the Zn-SPs-added scaffolds promoted the osteogenic differentiation and mineralization of BMSCs most likely because of the release of Zn^{2+} from the degradation of Zn-SPs [56,57]. But if Zn^{2+} can't maintained at a certain concentration, the osteogenic activity will be weakened. It was confirmed that the expression of ALP and Col I were up-regulated when BMSCs were cultured in the medium with a Zn^{2+} concentration of 3.2 nM on the 7th day, but were down-regulated on the 14th day [58]. In contrast, PTZ scaffold that we designed achieved a long-term stable release of Zn^{2+} , and highly expressed ALP, Runx2, Col I, OPN and OCN until 14 days, indicating that this promoting osteogenic effect was sustained. While Runx2 is the main regulator of the other osteogenic markers mentioned above [59].

It has been noted that Zn^{2+} affect the osteogenic activity through the expression of Runx2, but the specific mechanism is unknown [60]. Therefore, we further explored the cellular pathway mechanism of BMSCs differentiation affected by PTZ scaffold. The expression of four proteins (BCL9L, FZD2, ENPP1 and HTRA1) directly related to β -catenin was up-regulated by proteomic analysis. β -Catenin is a key target of the Wnt/ β -catenin signaling pathway [61], and we speculated that the Wnt/ β -catenin signaling pathway might play an important role in promotion of osteogenic differentiation and mineralization of BMSCs affected by PTZ scaffolds. Among the four proteins, the increased activity of FZD2 could explain the activation of Wnt/ β -catenin signaling pathway [62]. Furthermore, ENPP1 and HTRA1 have been shown closely related to osteogenesis and are present downstream of Runx2 [63–65]. In this study, we found that Runx2 and its downstream targets

ALP, Col I, OPN, OCN, ENPP1, HTRA1 and other proteins were highly expressed when BMSCs cultured with PTZ scaffolds. We also found that although the expression of the vascularization related proteins SNTB1 and ARNT was up-regulated, but the VEGF pathway that plays an angiogenic role in bone repair [66] might not be activated. Interestingly, the up-regulation of the anti-inflammatory related protein CCN2 and the down-regulation of the pro-inflammatory related proteins IL1RN and EIF2AK2 might indicate the activation of P38 MAPK pathway and the inhibition of NF κ B pathway, resulting in an immune microenvironment favorable for osteogenesis [67,68]. The anti-inflammatory effect might also related to Zn^{2+} release [69]. However, the specific cellular mechanism of Zn^{2+} induces osteogenic differentiation of BMSCs through Wnt/ β -catenin signaling pathway has not been clarified in previous studies. Our study speculated that the specific cellular mechanism of promoting the osteogenic differentiation might be that the generated Zn^{2+} activated the receptor FZD2 on the membrane of BMSCs, and then Wnt/ β -catenin pathway is activated, resulting in the up-regulation of Runx2 protein in nucleus. Subsequently, the downstream proteins of ENPP1, HTRA1, ALP, Col I, OPN and OCN was up-regulated, which promoted the osteogenic differentiation process (Fig. 5f).

Finally, *in vivo* experiments were carried out to reconfirm our hypothesis about the cellular mechanism. The added of Zn-SPs formed more new bone compared to the other groups, and the most likely reason was that Zn-SPs accelerated osteogenic differentiation and mineralization. The new formed bone was grew from the periphery to the inside of scaffold due to the pore connectivity and macroporous structure. The good osteoconductivity of the scaffold was demonstrated by the growth of new bone into the interior of the scaffold. Most importantly, the new formed bone in PTZ group was more dense than other groups, indicating the Zn^{2+} released from PTZ enhanced the osteoinductivity of scaffolds. We also observed that PTZ group formed the largest amount of new bone tissue by histological staining than that in PT group, and this scaffold have less fibrous tissue formation. Those may be related to the anti-inflammatory effect of PTZ scaffold found in *in vitro* experiments. During bone regeneration progress, severe inflammatory response and excessive fibrous tissue formation hinder the bone regeneration [70,71]. Some studies have pointed out that Zn^{2+} can regulate the bone immune microenvironment in the early stage of osteogenesis to achieve good bone regeneration effect [72,73]. To further elucidate the mechanism by which PTZ scaffolds promote bone regeneration and anti-inflammatory, we detected the expressions of osteogenesis-related proteins BMP2, OPN, anti-inflammatory related protein IL-10 and pro-inflammatory related protein TNF- α in bone tissue. After addition of Zn-SPs, BMP2 and OPN were upregulated at 4th, 8th, and 12th week, indicating the long-term osteogenic-promoting ability. We also found that the expression of IL-10 and TNF- α increased over time after PTZ implantation, indicating the persistence of immune response. This is essential in the process of bone tissue repair [74]. The expression of IL-10 was higher in PTZ group at 4, 8 and 12 weeks compared to the other three groups, while the expression of TNF- α was lower, indicating a sustained anti-inflammatory effect after the addition of Zn-SPs. Moreover, the M1 phenotype of macrophages was higher in PTZ group than the other two groups, further proving the existence of anti-inflammatory properties of PTZ scaffolds. While it has been confirmed that BMP2 can promote osteogenic differentiation of BMSCs by increasing the expression of Wnt ligand protein and β -catenin protein [75,76]. IL-10 can also form an immune microenvironment favorable for the osteogenic differentiation of BMSCs by activating the P38 MAPK pathway and inhibiting the NF κ B pathway [77]. Therefore, we concluded that the cellular mechanism of PTZ scaffold promoting bone regeneration is through activate the Wnt/ β -catenin signaling pathway, and exhibit anti-inflammatory effect by activating P38 MAPK pathway and inhibiting NF κ B pathway.

5. Conclusion

In summary, we used LT-RP 3D printing technology to add Zn-SPs to

PLGA/ β -TCP for bone repair. The printed PTZ scaffold had a bionic structure with improved mechanical, osteoinductive and anti-inflammatory properties. After adding 1 wt% Zn-SPs to PLGA/ β -TCP, the PTZ scaffold produced cytocompatibility and was able to release a safe dose of Zn²⁺ for 16 weeks to ensure long-term non-cytotoxicity. At the same time, the multi-level pore structure generated by added Zn-SPs mimicked cancellous bone, which was beneficial to the ingrowth and osteogenic differentiation of BMSCs. The PTZ scaffold had a Young's modulus of 63.41 ± 1.89 MPa and compressive strength of 2.887 ± 0.025 MPa, which were close to cancellous bone. In addition, the addition of Zn-SPs had no adverse effects on the viability and proliferation of BMSCs, but also promoted their adhesion and osteogenic differentiation, and exhibited anti-inflammatory properties *in vivo*. We also found that PTZ promoted bone regeneration by activating the Wnt/ β -catenin signaling pathway, and achieved anti-inflammatory effects by activating the P38 MAPK pathway and inhibiting the NF κ B pathway. The addition of Zn-SPs made up for the deficiencies of PLGA/ β -TCP scaffolds in mechanical, osteoinductive and anti-inflammatory properties. This study can lay the foundation for the subsequent study of bone regeneration mechanism of Zn-containing biomaterials, which is expected to be a new strategy for clinical treatment of bone defects.

CRedit authorship contribution statement

Chunxu Li: Conceptualization, Methodology, Investigation, Writing – original draft, Data curation. **Fengbo Sun:** Conceptualization, Methodology, Investigation, Writing – review & editing. **Jingjing Tian:** Conceptualization, Methodology, Writing – review & editing. **Jiahao Li:** Methodology, Investigation. **Haidan Sun:** Data curation. **Yong Zhang:** Investigation. **Shigong Guo:** Writing – review & editing. **Yuanhua Lin:** Investigation. **Xiaodan Sun:** Conceptualization, Methodology, Resources, Supervision, Project administration, Writing – review & editing. **Yu Zhao:** Conceptualization, Methodology, Resources, Supervision, Writing – review & editing, Project administration, Funding acquisition.

Declaration of competing interest

The authors declare that they have no known competing financial interests or personal relationships that could have appeared to influence the work reported in this paper.

Acknowledgments

This work was supported by Tsinghua University-Peking Union Medical College Hospital Initiative Scientific Research Program (20191080871) and the National Natural Science Foundation of China (82272464, 82002314).

Appendix A. Supplementary data

Supplementary data to this article can be found online at <https://doi.org/10.1016/j.bioactmat.2022.12.015>.

References

- M. Li, X. Xing, H. Huang, C. Liang, X. Gao, Q. Tang, X. Xu, J. Yang, L. Liao, W. Tian, BMSC-derived ApoEVs promote craniofacial bone repair via ROS/JNK signaling, *J. Dent. Res.* 101 (6) (2022) 714–723, <https://doi.org/10.1177/00220345211068338>.
- J.B. Park, J.H. Yang, D.G. Chang, S.I. Suk, S.W. Suh, G.U. Kim, J.Y. Choi, J.Y. Seo, H.Y. Park, S.I. Kim, Y.H. Kim, K.Y. Ha, Comparison of union rates between autogenous iliac crest bone graft and local bone graft as fusion materials in lumbar fusion surgery: an evaluation of up to 3-level fusion, *World Neurosurg* 139 (2020) e286–e292, <https://doi.org/10.1016/j.wneu.2020.03.211>.
- M.K. Jacobsen, A.K. Andresen, A.B. Jespersen, C. Stottstrup, L.Y. Carreon, S. Overgaard, M.O. Andersen, Randomized double blind clinical trial of ABM/P-15 versus allograft in noninstrumented lumbar fusion surgery, *Spine J.* 20 (5) (2020) 677–684, <https://doi.org/10.1016/j.spinee.2020.01.009>.
- M. Zhang, J.P. Matinlinna, J.K.H. Tsoi, W. Liu, X. Cui, W.W. Lu, H. Pan, Recent developments in biomaterials for long-bone segmental defect reconstruction: a narrative overview, *J Orthop Translat* 22 (2020) 26–33, <https://doi.org/10.1016/j.jot.2019.09.005>.
- J. Kulkova, N. Moritz, E.O. Suokas, N. Strandberg, K.A. Leino, T.T. Laitio, H.T. Aro, Osteointegration of PLGA implants with nanostructured or micro-sized beta-TCP particles in a minipig model, *J. Mech. Behav. Biomed. Mater.* 40 (2014) 190–200, <https://doi.org/10.1016/j.jmbbm.2014.08.028>.
- W. Hao, L. Pang, M. Jiang, R. Lv, Z. Xiong, Y.Y. Hu, Skeletal repair in rabbits using a novel biomimetic composite based on adipose-derived stem cells encapsulated in collagen I gel with PLGA-beta-TCP scaffold, *J. Orthop. Res.* 28 (2) (2010) 252–257, <https://doi.org/10.1002/jor.20969>.
- F.A. Barber, D.B. Spenciner, S. Bhattacharyya, L.E. Miller, Biocomposite implants composed of poly(lactide-co-glycolide)/beta-tricalcium phosphate: systematic review of imaging, complication, and performance outcomes, *Arthroscopy* 33 (3) (2017) 683–689, <https://doi.org/10.1016/j.arthro.2016.09.032>.
- Y. Zhang, C. Wang, L. Fu, S. Ye, M. Wang, Y. Zhou, Fabrication and application of novel porous scaffold in situ-loaded graphene oxide and osteogenic peptide by cryogenic 3D printing for repairing critical-sized bone defect, *Molecules* 24 (9) (2019), <https://doi.org/10.3390/molecules24091669>.
- S.K. Lee, C.M. Han, W. Park, I.H. Kim, Y.K. Joung, D.K. Han, Synergistically enhanced osteoconductivity and anti-inflammation of PLGA/beta-TCP/Mg(OH)(2) composite for orthopedic applications, *Mater Sci Eng C Mater Biol Appl* 94 (2019) 65–75, <https://doi.org/10.1016/j.msec.2018.09.011>.
- J. Liu, B. Liu, S. Min, B. Yin, B. Peng, Z. Yu, C. Wang, X. Ma, P. Wen, Y. Tian, Y. Zheng, Biodegradable magnesium alloy WE43 porous scaffolds fabricated by laser powder bed fusion for orthopedic applications: process optimization, *in vitro* and *in vivo* investigation, *Bioact. Mater.* 16 (2022) 301–319, <https://doi.org/10.1016/j.bioactmat.2022.02.020>.
- D. Xia, Y. Qin, H. Guo, P. Wen, H. Lin, M. Voshage, J. H. Schleifenbaum, Y. Cheng and Y. Zheng: Additively manufactured pure zinc porous scaffolds for critical-sized bone defects of rabbit femur. *Bioact. Mater.*, 19, 12–23 (2023) doi:10.1016/j.bioactmat.2022.03.010.
- Z. Zhang, B. Jia, H. Yang, Y. Han, Q. Wu, K. Dai, Y. Zheng, Zn0.8Li0.1Sr-a biodegradable metal with high mechanical strength comparable to pure Ti for the treatment of osteoporotic bone fractures: *in vitro* and *in vivo* studies, *Biomaterials* 275 (2021), 120905, <https://doi.org/10.1016/j.biomaterials.2021.120905>.
- H. Yang, B. Jia, Z. Zhang, X. Qu, G. Li, W. Lin, D. Zhu, K. Dai, Y. Zheng, Alloying design of biodegradable zinc as promising bone implants for load-bearing applications, *Nat. Commun.* 11 (1) (2020) 401, <https://doi.org/10.1038/s41467-019-14153-7>.
- Z. Zhang, B. Jia, H. Yang, Y. Han, Q. Wu, K. Dai, Y. Zheng, Biodegradable ZnLiCa ternary alloys for critical-sized bone defect regeneration at load-bearing sites: *in vitro* and *in vivo* studies, *Bioact. Mater.* 6 (11) (2021) 3999–4013, <https://doi.org/10.1016/j.bioactmat.2021.03.045>.
- Y. Lai, Y. Li, H. Cao, J. Long, X. Wang, L. Li, C. Li, Q. Jia, B. Teng, T. Tang, J. Peng, D. Eglin, M. Alini, D.W. Grijpma, G. Richards, L. Qin, Osteogenic magnesium incorporated into PLGA/TCP porous scaffold by 3D printing for repairing challenging bone defect, *Biomaterials* 197 (2019) 207–219, <https://doi.org/10.1016/j.biomaterials.2019.01.013>.
- Y. Li, Q. Pan, J. Xu, X. He, H.A. Li, D.A. Oldridge, G. Li, L. Qin, Overview of methods for enhancing bone regeneration in distraction osteogenesis: potential roles of biomaterials, *J Orthop Translat* 27 (2021) 110–118, <https://doi.org/10.1016/j.jot.2020.11.008>.
- B. Li, C. Ruan, Y. Ma, Z. Huang, Z. Huang, G. Zhou, J. Zhang, H. Wang, Z. Wu, G. Qiu, Fabrication of vascularized bone flaps with sustained release of recombinant human bone morphogenetic protein-2 and arteriovenous bundle, *Tissue Eng.* 24 (17–18) (2018) 1413–1422, <https://doi.org/10.1089/ten.tea.2018.0002>.
- T. Yoshida, H. Miyaji, K. Otani, K. Inoue, K. Nakane, H. Nishimura, A. Ibara, A. Shimada, K. Ogawa, E. Nishida, T. Sugaya, L. Sun, B. Fugetsu, M. Kawanami, Bone augmentation using a highly porous PLGA/beta-TCP scaffold containing fibroblast growth factor-2, *J. Periodontol. Res.* 50 (2) (2015) 265–273, <https://doi.org/10.1111/jre.12206>.
- E.J. Carragee, E.L. Hurwitz, B.K. Weiner, A critical review of recombinant human bone morphogenetic protein-2 trials in spinal surgery: emerging safety concerns and lessons learned, *Spine J.* 11 (6) (2011) 471–491, <https://doi.org/10.1016/j.spinee.2011.04.023>.
- S.J.M.S. Virtanen, Engineering: biodegradable Mg and Mg alloys, *Corrosion and biocompatibility* 176 (20) (2011) 1600–1608, <https://doi.org/10.1016/j.mseb.2011.05.028>.
- G. Li, H. Yang, Y. Zheng, X.H. Chen, J.A. Yang, D. Zhu, L. Ruan, K. Takashima, Challenges in the use of zinc and its alloys as biodegradable metals: perspective from biomechanical compatibility, *Acta Biomater.* 97 (2019) 23–45, <https://doi.org/10.1016/j.actbio.2019.07.038>.
- R.A. Bozym, F. Chimienti, L.J. Giblin, G.W. Gross, I. Korichneva, Y. Li, S. Libert, W. Maret, M. Parviz, C.J. Frederickson, R.B. Thompson, Free zinc ions outside a narrow concentration range are toxic to a variety of cells *in vitro*, *Exp. Biol. Med.* 235 (6) (2010) 741–750, <https://doi.org/10.1258/ebm.2010.009258>.
- Y. Li, W. Xiong, C. Zhang, B. Gao, H. Guan, H. Cheng, J. Fu, F. Li, Enhanced osseointegration and antibacterial action of zinc-loaded titania-nanotube-coated titanium substrates: *in vitro* and *in vivo* studies, *J. Biomed. Mater. Res.* 102 (11) (2014) 3939–3950, <https://doi.org/10.1002/jbm.a.35060>.
- U. Aydemir Sezer, K. Ozturk, B. Aru, G. Yanikkaya Demirel, S. Sezer, M.R. Bozkurt, Zero valent zinc nanoparticles promote neuroglial cell proliferation: a

- biodegradable and conductive filler candidate for nerve regeneration, *J. Mater. Sci. Mater. Med.* 28 (1) (2017) 19, <https://doi.org/10.1007/s10856-016-5831-1>.
- [25] J.C. Forero, E. Roa, J.G. Reyes, C. Acevedo, N. Osses, Development of useful biomaterial for bone tissue engineering by incorporating nano-copper-zinc alloy (nCuZn) in chitosan/gelatin/nano-hydroxyapatite (ch/G/nHAp) scaffold, *Materials* 10 (10) (2017), <https://doi.org/10.3390/ma10101177>.
- [26] T.W. Sun, W.L. Yu, Y.J. Zhu, F. Chen, Y.G. Zhang, Y.Y. Jiang, Y.H. He, Porous nanocomposite comprising ultralong hydroxyapatite nanowires decorated with zinc-containing nanoparticles and chitosan: synthesis and application in bone defect repair, *Chemistry* 24 (35) (2018) 8809–8821, <https://doi.org/10.1002/chem.201800425>.
- [27] X. Huang, D. Huang, T. Zhu, X. Yu, K. Xu, H. Li, H. Qu, Z. Zhou, K. Cheng, W. Wen, Z. Ye, Sustained zinc release in cooperation with CaP scaffold promoted bone regeneration via directing stem cell fate and triggering a pro-healing immune stimuli, *J. Nanobiotechnol.* 19 (1) (2021) 207, <https://doi.org/10.1186/s12951-021-00956-8>.
- [28] Y. Qin, P. Wen, H. Guo, D. Xia, Y. Zheng, L. Jauer, R. Poprawe, M. Voshage, J. H. Schleifenbaum, Additive manufacturing of biodegradable metals: current research status and future perspectives, *Acta Biomater.* 98 (2019) 3–22, <https://doi.org/10.1016/j.actbio.2019.04.046>.
- [29] G. Qian, L. Zhang, G. Wang, Z. Zhao, S. Peng, C. Shuai, 3D printed Zn-doped mesoporous silica-incorporated poly-L-lactic acid scaffolds for bone repair, *Int J Bioprint* 7 (2) (2021) 346, <https://doi.org/10.18063/ijb.v7i2.346>.
- [30] G. Asensio, L. Benito-Garzon, R.A. Ramirez-Jimenez, Y. Guadilla, J. Gonzalez-Rubio, C. Abradelo, J. Parra, M.R. Martin-Lopez, M.R. Aguilar, B. Vazquez-Lasa, L. Rojo, Biomimetic gradient scaffolds containing hyaluronic acid and Sr/Zn folates for osteochondral tissue engineering, *Polymers* 14 (1) (2021), <https://doi.org/10.3390/polym14010012>.
- [31] S. Wang, R. Li, D. Xia, X. Zhao, Y. Zhu, R. Gu, J. Yoon, Y. Liu, The impact of Zn-doped synthetic polymer materials on bone regeneration: a systematic review, *Stem Cell Res. Ther.* 12 (1) (2021) 123, <https://doi.org/10.1186/s13287-021-02195-y>.
- [32] Y. Gu, Y. Sun, S. Shujaat, A. Braem, C. Politis, R. Jacobs, 3D-printed porous Ti6Al4V scaffolds for long bone repair in animal models: a systematic review, *J. Orthop. Surg. Res.* 17 (1) (2022) 68, <https://doi.org/10.1186/s13018-022-02960-6>.
- [33] X.H. Xie, X.L. Wang, G. Zhang, Y.X. He, Y. Leng, T.T. Tang, X. Pan, L. Qin, Biofabrication of a PLGA-TCP-based porous bioactive bone substitute with sustained release of icaritin, *J Tissue Eng Regen Med* 9 (8) (2015) 961–972, <https://doi.org/10.1002/term.1679>.
- [34] M. Chen, Y. Zhang, P. Zhou, X. Liu, H. Zhao, X. Zhou, Q. Gu, B. Li, X. Zhu, Q. Shi, Substrate stiffness modulates bone marrow-derived macrophage polarization through NF-kappaB signaling pathway, *Bioact. Mater.* 5 (4) (2020) 880–890, <https://doi.org/10.1016/j.bioactmat.2020.05.004>.
- [35] P. Kazmierczak, J. Golus, J. Kolmas, M. Wojcik, D. Kolodnynska, A. Przekora, Noncytotoxic zinc-doped nanohydroxyapatite-based bone scaffolds with strong bactericidal, bacteriostatic, and antibiofilm activity, *Biomater Adv* 139 (2022), 213011, <https://doi.org/10.1016/j.bioadv.2022.213011>.
- [36] A. Tripathi, S. Saravanan, S. Pattnaik, A. Moorthi, N.C. Partridge, N. Selvamurugan, Bio-composite scaffolds containing chitosan/nano-hydroxyapatite/nano-copper-zinc for bone tissue engineering, *Int. J. Biol. Macromol.* 50 (1) (2012) 294–299, <https://doi.org/10.1016/j.ijbiomac.2011.11.013>.
- [37] M.R. Badr-Mohammadi, S. Hesarak, A. Zamanian, Mechanical properties and in vitro cellular behavior of zinc-containing nano-bioactive glass doped biphasic calcium phosphate bone substitutes, *J. Mater. Sci. Mater. Med.* 25 (1) (2014) 185–197, <https://doi.org/10.1007/s10856-013-5062-7>.
- [38] X. Yuan, T. Lu, F. He, T. Wu, X. Wang, J. Ye, 3D-plotted zinc silicate/beta-tricalcium phosphate ceramic scaffolds enable fast osteogenesis by activating the p38 signaling pathway, *J. Mater. Chem. B* 10 (46) (2022) 9639–9653, <https://doi.org/10.1039/d2tb01868c>.
- [39] X. Fu, Y. Li, T. Huang, Z. Yu, K. Ma, M. Yang, Q. Liu, H. Pan, H. Wang, J. Wang, M. Guan, Runx2/Osterix and zinc uptake synergize to orchestrate osteogenic differentiation and citrate containing bone apatite formation, *Adv. Sci.* 5 (4) (2018), 1700755, <https://doi.org/10.1002/adv.201700755>.
- [40] T. Koga, S. Kumazawa, Y. Okimura, Y. Zaitus, K. Umeshita, I. Asahina, Evaluation of poly lactic-co-glycolic acid-coated beta-tricalcium phosphate bone substitute as a graft material for ridge preservation after tooth extraction in dog mandible: a comparative study with conventional beta-tricalcium phosphate granules, *Materials* 13 (16) (2020), <https://doi.org/10.3390/ma13163452>.
- [41] Y. Nakano, M. Shimoda, S. Okudomi, S. Kawaraya, M. Kawahara, K.I. Tanaka, Seleno-l-methionine suppresses copper-enhanced zinc-induced neuronal cell death via induction of glutathione peroxidase, *Metallomics* 12 (11) (2020) 1693–1701, <https://doi.org/10.1039/d0mt00136h>.
- [42] A.M. Holmes, L. Mackenzie, M.S. Roberts, Disposition and measured toxicity of zinc oxide nanoparticles and zinc ions against keratinocytes in cell culture and viable human epidermis, *Nanotoxicology* 14 (2) (2020) 263–274, <https://doi.org/10.1080/17435390.2019.1692382>.
- [43] D. Liang, M. Yang, B. Guo, J. Cao, L. Yang, X. Guo, Zinc upregulates the expression of osteoprotegerin in mouse osteoblasts MC3T3-E1 through PKC/MAPK pathways, *Biol. Trace Elem. Res.* 146 (3) (2012) 340–348, <https://doi.org/10.1007/s12011-011-9254-z>.
- [44] N. Contessi Negrini, C. Ricci, F. Bongiorno, L. Trombi, D. D'Alessandro, S. Danti, S. Fare, An osteosarcoma model by 3D printed polyurethane scaffold and in vitro generated bone extracellular matrix, *Cancers* 14 (8) (2022), <https://doi.org/10.3390/cancers14082003>.
- [45] H. Xia, L. Dong, M. Hao, Y. Wei, J. Duan, X. Chen, L. Yu, H. Li, Y. Sang, H. Liu, Osteogenic property regulation of stem cells by a hydroxyapatite 3D-hybrid scaffold with cancellous bone structure, *Front. Chem.* 9 (2021), 798299, <https://doi.org/10.3389/fchem.2021.798299>.
- [46] M. Stiehler, C. Bunger, A. Baatrup, M. Lind, M. Kassem, T. Mygind, Effect of dynamic 3-D culture on proliferation, distribution, and osteogenic differentiation of human mesenchymal stem cells, *J. Biomed. Mater. Res.* 89 (1) (2009) 96–107, <https://doi.org/10.1002/jbm.a.31967>.
- [47] J. Zhang, X. Luo, D. Barbieri, A.M. Barradas, J.D. de Bruijn, C.A. van Blitterswijk, H. Yuan, The size of surface microstructures as an osteogenic factor in calcium phosphate ceramics, *Acta Biomater.* 10 (7) (2014) 3254–3263, <https://doi.org/10.1016/j.actbio.2014.03.021>.
- [48] Z. Wood, L. Lynn, J.T. Nguyen, M.A. Black, M. Patel, M.M. Barak, Are we crying Wolff? 3D printed replicas of trabecular bone structure demonstrate higher stiffness and strength during off-axis loading, *Bone* 127 (2019) 635–645, <https://doi.org/10.1016/j.bone.2019.08.002>.
- [49] C. Pan, X. Sun, G. Xu, Y. Su, D. Liu, The effects of beta-TCP on mechanical properties, corrosion behavior and biocompatibility of beta-TCP/Zn-Mg composites, *Mater Sci Eng C Mater Biol Appl* 108 (2020), 110397, <https://doi.org/10.1016/j.msec.2019.110397>.
- [50] C.J. Hernandez, G.S. Beaupre, T.S. Keller, D.R. Carter, The influence of bone volume fraction and ash fraction on bone strength and modulus, *Bone* 29 (1) (2001) 74–78, [https://doi.org/10.1016/s8756-3282\(01\)00467-7](https://doi.org/10.1016/s8756-3282(01)00467-7).
- [51] X. Li, M. Wang, W. Zhang, Y. Bai, Y. Liu, J. Meng, L. Zhang, A magnesium-incorporated nanoporous titanium coating for rapid osseointegration, *Int. J. Nanomed.* 15 (2020) 6593–6603, <https://doi.org/10.2147/IJN.S255486>.
- [52] Y. Li, P. Aavanram, J. Zhou, K. Lietaert, F.S.L. Bobbert, Y. Kubo, M.A. Leeftang, H. Jahr, A.A. Zadpoor, Additively manufactured functionally graded biodegradable porous zinc, *Biomater. Sci.* 8 (9) (2020) 2404–2419, <https://doi.org/10.1039/c9bm01904a>.
- [53] M.T. Raimondi, S.M. Eaton, M. Lagana, V. Aprile, M.M. Nava, G. Cerullo, R. Osellame, Three-dimensional structural niches engineered via two-photon laser polymerization promote stem cell homing, *Acta Biomater.* 9 (1) (2013) 4579–4584, <https://doi.org/10.1016/j.actbio.2012.08.022>.
- [54] G. Mendonca, D.B. Mendonca, F.J. Aragao, L.F. Cooper, Advancing dental implant surface technology—from micron- to nanotopography, *Biomaterials* 29 (28) (2008) 3822–3835, <https://doi.org/10.1016/j.biomaterials.2008.05.012>.
- [55] D. Lin, Y. Chai, Y. Ma, B. Duan, Y. Yuan, C. Liu, Rapid initiation of guided bone regeneration driven by spatiotemporal delivery of IL-8 and BMP-2 from hierarchical MBG-based scaffold, *Biomaterials* 196 (2019) 122–137, <https://doi.org/10.1016/j.biomaterials.2017.11.011>.
- [56] C. He, Y. Hu, L. Yin, C. Tang, C. Yin, Effects of particle size and surface charge on cellular uptake and biodistribution of polymeric nanoparticles, *Biomaterials* 31 (13) (2010) 3657–3666, <https://doi.org/10.1016/j.biomaterials.2010.01.065>.
- [57] D.L. Thorek, A. Tsourkas, Size, charge and concentration dependent uptake of iron oxide particles by non-phagocytic cells, *Biomaterials* 29 (26) (2008) 3583–3590, <https://doi.org/10.1016/j.biomaterials.2008.05.015>.
- [58] K. Yusa, O. Yamamoto, M. Fukuda, S. Koyota, Y. Koizumi, T. Sugiyama, In vitro prominent bone regeneration by release zinc ion from Zn-modified implant, *Biochem. Biophys. Res. Commun.* 412 (2) (2011) 273–278, <https://doi.org/10.1016/j.bbrc.2011.07.082>.
- [59] J.M. Kim, Y.S. Yang, K.H. Park, X. Ge, R. Xu, N. Li, M. Song, H. Chun, S. Bok, J. F. Charles, O. Filhol-Cochet, B. Boldyreff, T. Dinter, P.B. Yu, N. Kon, W. Gu, T. Takarada, M.B. Greenblatt, J.H. Shim, A RUNX2 stabilization pathway mediates physiologic and pathologic bone formation, *Nat. Commun.* 11 (1) (2020) 2289, <https://doi.org/10.1038/s41467-020-16038-6>.
- [60] I.S. Kwon, Y.E. Cho, R.A. Lomedha, H.I. Shin, J.Y. Choi, Y.H. Kang, J.H. Beattie, Zinc deficiency suppresses matrix mineralization and retards osteogenesis transiently with catch-up possibly through Runx 2 modulation, *Bone* 46 (3) (2010) 732–741, <https://doi.org/10.1016/j.bone.2009.11.003>.
- [61] B.T. MacDonald, K. Tamai, X. He, Wnt/beta-catenin signaling: components, mechanisms, and diseases, *Dev. Cell* 17 (1) (2009) 9–26, <https://doi.org/10.1016/j.devcel.2009.06.016>.
- [62] X. Sun, Z. Cao, Q. Zhang, S. Liu, F. Xu, J. Che, Y. Zhu, Y. Li, C. Pan, W. Liang, Aluminum trichloride impairs bone and downregulates Wnt/beta-catenin signaling pathway in young growing rats, *Food Chem. Toxicol.* 86 (2015) 154–162, <https://doi.org/10.1016/j.fct.2015.10.005>.
- [63] M.M. Gao, Q.N. Su, T.Z. Liang, J.X. Ma, T.Z. Liang, M.J. Stoddart, R.G. Richards, Z. Y. Zhou, N.X. Zou, Transcriptional activation of ENPP1 by osterix in osteoblasts and osteocytes, *Eur. Cell. Mater.* 36 (2018) 1–14, <https://doi.org/10.22203/eCM.v036a01>.
- [64] A.N. Tiaden, M. Breiden, A. Mirsaidi, F.A. Weber, G. Bahrenberg, S. Glanz, P. Cinelli, M. Ehrmann, P.J. Richards, Human serine protease HTRA1 positively regulates osteogenesis of human bone marrow-derived mesenchymal stem cells and mineralization of differentiating bone-forming cells through the modulation of extracellular matrix protein, *Stem Cell.* 30 (10) (2012) 2271–2282, <https://doi.org/10.1002/stem.1190>.
- [65] P.P.R. Iyyanar, M.P. Thangaraj, B.F. Eames, A.J. Nazarali, Htra1 is a novel transcriptional target of RUNX2 that promotes osteogenic differentiation, *Cell. Physiol. Biochem.* 53 (5) (2019) 832–850, <https://doi.org/10.33594/000000176>.
- [66] K. Hu, B.R. Olsen, Osteoblast-derived VEGF regulates osteoblast differentiation and bone formation during bone repair, *J. Clin. Invest.* 126 (2) (2016) 509–526, <https://doi.org/10.1172/JCI82585>.
- [67] Y. Song, H. Wu, Y. Gao, J. Li, K. Lin, B. Liu, X. Lei, P. Cheng, S. Zhang, Y. Wang, J. Sun, L. Bi, G. Pei, Zinc silicate/nano-hydroxyapatite/collagen scaffolds promote angiogenesis and bone regeneration via the p38 MAPK pathway in activated

- monocytes, *ACS Appl. Mater. Interfaces* 12 (14) (2020) 16058–16075, <https://doi.org/10.1021/acscami.0c00470>.
- [68] Y. Wang, Y. Liu, M. Zhang, L. Lv, X. Zhang, P. Zhang, Y. Zhou, Inhibition of PTGS1 promotes osteogenic differentiation of adipose-derived stem cells by suppressing NF- κ B signaling, *Stem Cell Res. Ther.* 10 (1) (2019) 57, <https://doi.org/10.1186/s13287-019-1167-3>.
- [69] Y. Kim, Y.J. Jeon, K. Ryu, T.Y. Kim, Zinc(II) ion promotes anti-inflammatory effects of rhSOD3 by increasing cellular association, *BMB Rep* 50 (2) (2017) 85–90, <https://doi.org/10.5483/bmbrep.2017.50.2.150>.
- [70] R.J. Miron, D.D. Bosshardt, OsteoMacs: key players around bone biomaterials, *Biomaterials* 82 (2016) 1–19, <https://doi.org/10.1016/j.biomaterials.2015.12.017>.
- [71] H. Fang, C. Luo, S. Liu, M. Zhou, Y. Zeng, J. Hou, L. Chen, S. Mou, J. Sun, Z. Wang, A biocompatible vascularized graphene oxide (GO)-collagen chamber with osteoinductive and anti-fibrosis effects promotes bone regeneration in vivo, *Theranostics* 10 (6) (2020) 2759–2772, <https://doi.org/10.7150/thno.42006>.
- [72] H. Sun, K. Zheng, T. Zhou, A.R. Boccacini, Incorporation of zinc into binary SiO₂-CaO mesoporous bioactive glass nanoparticles enhances anti-inflammatory and osteogenic activities, *Pharmaceutics* 13 (12) (2021), <https://doi.org/10.3390/pharmaceutics13122124>.
- [73] W. Liu, J. Li, M. Cheng, Q. Wang, K.W.K. Yeung, P.K. Chu, X. Zhang, Zinc-Modified sulfonated polyetheretherketone surface with immunomodulatory function for guiding cell fate and bone regeneration, *Adv. Sci.* 5 (10) (2018), 1800749, <https://doi.org/10.1002/advs.201800749>.
- [74] Y. Niu, Z. Wang, Y. Shi, L. Dong, C. Wang, Modulating macrophage activities to promote endogenous bone regeneration: biological mechanisms and engineering approaches, *Bioact. Mater.* 6 (1) (2021) 244–261, <https://doi.org/10.1016/j.bioactmat.2020.08.012>.
- [75] N. Itasaki, S. Hoppler, Crosstalk between Wnt and bone morphogenic protein signaling: a turbulent relationship, *Dev. Dynam.* 239 (1) (2010) 16–33, <https://doi.org/10.1002/dvdy.22009>.
- [76] J.H. Lee, B.G. Kim, J.M. Ahn, H.J. Park, S.K. Park, J.S. Yoo, J.R. Yates 3rd, J.Y. Cho, Role of PI3K on the regulation of BMP2-induced beta-Catenin activation in human bone marrow stem cells, *Bone* 46 (6) (2010) 1522–1532, <https://doi.org/10.1016/j.bone.2010.02.013>.
- [77] E. Chen, G. Liu, X. Zhou, W. Zhang, C. Wang, D. Hu, D. Xue, Z. Pan, Concentration-dependent, dual roles of IL-10 in the osteogenesis of human BMSCs via P38/MAPK and NF- κ B signaling pathways, *Faseb. J.* 32 (9) (2018) 4917–4929, <https://doi.org/10.1096/fj.201701256RRR>.